



TEKNILLINEN KORKEAKOULU
Teknillisen fysiikan ja
matematiikan osasto

Markus Airila

Electron Energy Spectra in Gyrotrons with Depressed Collectors

Master's thesis submitted in partial fulfillment of the requirements
for the degree of Master of Science in Technology

Espoo, 27th November 2000

Supervisor: Professor Rainer Salomaa
Instructor: Olgierd Dumbrajs, Ph.D.

TEKNILLINEN KORKEAKOULU
TEKNILLISEN FYSIIKAN KIRJASTO
RAKENTAMALLINEN 2 C
02150 ESPOO

Author: Markus Airila Department: Department of engineering physics and mathematics Major subject: Engineering physics Minor subject: Mathematics	
Title: Electron Energy Spectra in Gyrotrons with Depressed Collectors Title in Finnish: Elektronien energiaspektrit hidastavalla kollektorilla varustetuissa gyrotroneissa Chair: Tfy-56 Engineering physics (Advanced Energy Systems) Supervisor: Prof. Rainer Salomaa Instructor: Olgierd Dumbrajs, Ph.D.	
<p>A depressed potential collector can give a major improvement to gyrotron efficiency and significantly suppress heat dissipation and x-ray generation at the collector surface. To use a depressed collector, the residual energies of the electron beam should be known, and the retarding potential chosen to be small enough. Electrons reflected by a too high potential would be trapped between the collector and the electron gun.</p> <p>The electron residual energies can be found using gyrotron theory whenever the solutions of the gyrotron equation are not chaotic. In this work the risk of chaotic electron trajectories in high efficiency operation of a gyrotron was studied by solving the gyrotron equation with several control parameter values. The specifically defined smoothness of the residual energy spectrum gives information about possible stochasticity of electron motion. It was found that the control parameter space can be divided into three different parts described by efficiency and the smoothness of the residual energy spectrum. The risk for chaos in the region of high efficiency turned out to be small. The results remained the same when spatial variation of the guiding magnetic field was allowed. The cold-cavity approximation, which was used in the computations, was found to be valid.</p> <p>A condition for electron trapping was derived in terms of the retarding voltage, and the effect of trapping was included in gyrotron efficiency computations. The results are presented as general efficiency contour plots in the control parameter plane. It was found that trapping seriously decreases the efficiency. The overall electron efficiency was calculated as a function of the retarding voltage for a representative set of control parameters including the effect of electron velocity spread. In most cases the trapping effect reduces the efficiency at collector voltages higher than 30–40 kV, the cathode voltage being 90 kV.</p>	
Number of pages: 66 Keywords: gyrotron, depressed collector, chaos, trapping, efficiency, velocity spread	
Department fills Approved: Library code:	

Tekijä: Markus Airila

Osasto: Teknillisen fysiikan ja matematiikan osasto

Pääaine: Teknillinen fysiikka

Sivuaine: Matematiikka

Työn nimi: Elektronien energiaspektrit hidastavalla kollektorilla varustetuissa gyrotroneissa

Title in English: Electron Energy Spectra in Gyrotrons with Depressed Collectors

Professuurin koodi ja nimi: Tfy-56 Teknillinen fysiikka (energiateknologiat)

Työn valvoja: Prof. Rainer Salomaa

Työn ohjaaja: Olgierd Dumbrajs, Ph.D.

Negatiivisessa potentiaalissa olevalla hidastavalla kollektorilla voidaan parantaa merkittävästi gyrotronin hyötysuhdetta sekä vähentää lämmöntuottoa ja röntgensäteilyä kollektorilla. Tällöin tulee tuntee elektronisuihkun jäännösenergiat ja valita niiden suhteen riittävän vähän hidastava potentiaali. Liian voimakkaan potentiaalin heijastamat elektronit loukkuuntuisivat kollektorin ja elektronitykin potentiaalien väliin.

Elektronien jäännösenergiat saadaan gyrotroniteoriasta, jos elektronien liikeyhtälön ratkaisut eivät ole kaoottisia. Tässä työssä tutkittiin kaaoksen mahdollisuutta käytetäessä gyrotronia korkealla hyötysuhteella. Tätä varten gyrotroneyhtälö ratkaistiin useilla eri ohjausparametrien arvoilla. Erityisesti määritellystä jäännösenergiaspektrin sileydestä voidaan päätellä mahdollinen elektronien liikkeen stokastisuus. Ilmeni, että ohjausparametriavaruus voidaan jakaa kolmeen erillaiseen alueeseen hyötysuhteen ja jäännösenergiaspektrin sileyden perusteella. Kaaoksen riski hyvän hyötysuhteen alueilla osoittautui vähäiseksi. Sama tulos saatiin käyttämällä resonaattorissa paikan suhteen muuttuvaa magneettikenttää. Laskuissa käytetty ”kylmän resonaattorin approksimaatio” todettiin toimivaksi.

Elektronien liikeyhtälön ratkaisuille johdettiin hidastavan potentiaalin avulla ilmaistava loukkuuntumisehto, ja gyrotronin hyötysuhteen laskenta laajennettiin ottamaan huomioon mahdollinen loukkuuntuminen. Saadut tulokset esitetään yleisinä hyötysuhteen tasa-arvokäyrinä ohjausparametritasossa. Havaittiin, että loukkuuntuminen heikentää hyötysuhdetta huomattavasti. Valituilla ohjausparametrien arvoilla saatava elektroni-hyötysuhde laskettiin hidastavan potentiaalin funktiona ottaen huomioon elektronien nopeushajonta. Useimmissa tapauksissa loukkuuntuminen heikentää hyötysuhdetta silloin, kun hidastava potentiaali on suurempi kuin 30–40 kV katodijännitteen ollessa 90 kV.

Sivumäärä: 66 Avainsanat: gyrotroni, hidastava kollektori, kaaos, loukkuuntuminen, hyötysuhde, nopeushajonta

Täytetään osastolla

Hyväksytty: Kirjasto:

Preface

This work was carried out in the Laboratory of Advanced Energy Systems at the Department of Engineering Physics and Mathematics at Helsinki University of Technology.

I am grateful to my instructor, Dr. Olgierd Dumbrajs, for his patience in teaching me during the course of this work. His invaluable guidance helped in the timely completion of the thesis. I also thank my supervisor, Professor Rainer Salomaa for providing me with the possibility to work in the laboratory. The laboratory staff has been most helpful in questions concerning computing and technical writing, as well as the physics itself. In particular, the suggestions given by Dr. Taina Kurki-Suonio have greatly improved the manuscript.

A special acknowledgment belongs to my wife Auli for her tireless encouragement. My parents Eeva and Mauri, and my grandparents Saimi and Soini have given a great contribution to my studies through their mental and financial support. My younger sister Kaisa—M.Sc. earlier this year—gave many practical hints at the very final stage of the work. Often a dynamic start of a productive workday has been an early breakfast run with my siblings Martta, Kerttu, and Hannu. Finally, I want to salute the teachers of Nikkari high school as persons who skillfully nourished the embryonic physicist in me.

Espoo, 27th November 2000,

A handwritten signature in blue ink, appearing to read 'Markus Airila', with a stylized, flowing script.

Markus Airila

Contents

1	Introduction	10
2	Gyrotrons	15
2.1	Operating principle	15
2.2	Electron gun	15
2.3	Interaction between electrons and the HF field	16
2.3.1	Electron motion in an electromagnetic field	16
2.3.2	Bunching mechanism in gyrotrons	17
2.3.3	Energy exchange between electrons and the HF field	19
2.3.4	Dispersion diagram of a gyrotron	19
2.3.5	Gyrotron equations	20
2.3.6	Efficiency of a gyrotron	23
3	Depressed Collectors	24
3.1	General about collectors in gyrotrons	24
3.2	Effect of a depressed collector on efficiency	24
3.3	Design issues	26
3.3.1	Conversion from rotational to axial energy	26
3.3.2	Collector geometry	27
3.3.3	Surface materials	28
3.4	Current status of development and future prospects	28
4	Electron Residual Energies	29
4.1	General	29
4.2	Definition of chaos	29
4.3	Possibility of chaotic electron trajectories in gyrotrons	30
4.4	Numerical evidence about chaos	30
4.5	Dependence of electron residual energy on initial conditions	32
4.5.1	Numerical codes	32
4.5.2	Smoothness of the energy spectrum	35
4.5.3	Efficiency-smoothness plots	36

5	Electron Trapping	41
5.1	General	41
5.2	Adiabatic and non-adiabatic trapping	41
5.3	Condition for electron trapping	42
5.4	Effects of electron trapping on perpendicular efficiency	44
5.4.1	General efficiency plots with inclusion of trapping . . .	44
5.4.2	Dependence of efficiency on collector potential	47
5.4.3	Space charge effects	53
6	Conclusions	54
6.1	Chaotic electron trajectories	54
6.2	Electron trapping	55
6.3	Recommendations	56
	Appendix A Flow Charts	61

List of Symbols

B	absolute value of magnetic field
\mathbf{B}	magnetic field
B_{cav}	axial magnetic field in interaction cavity
B_{coll}	axial magnetic field in collector
C_F^β	constant factor involved in F
C_Δ^β	constant factor involved in Δ
C_μ^β	constant factor involved in μ
c	speed of light in vacuum
\mathbf{E}	electric field
$-e$	charge of electron
F	beam-wave coupling factor
F_ϵ^β	corrected coupling factor: $F \rightarrow F_\epsilon^\beta$ as $\beta_{\perp 0} \rightarrow \beta_{\perp 0}(1 + \epsilon)$
F_ω	real part of frequency corresponding to angular frequency ω
f	dimensionless axial field profile function
\tilde{f}	transformed field profile function
f_e	velocity distribution function
I	dimensionless current
I_0	current
I_j	current on j th collector stage
i	imaginary unit
$k_{ }$	axial component of wave number
k_{\perp}	transverse component of wave number
L	length of interaction cavity
m_e	rest mass of electron
n	particle density
n, n_1, n_2	numbers of different initial conditions in numerical computations
P	power consumption
P_b	beam power
P_{coll}	power recovered by collector
P_{RF}	radio-frequency output power

p	complex transverse momentum in units of $\mathcal{P}_{\perp 0}$
\mathbf{p}	momentum
p_0	initial complex transverse momentum in units of $\mathcal{P}_{\perp 0}$
$p_{\text{cut-off}}$	"cut-off" parameter
p_{out}	complex dimensionless transverse momentum at cavity end
p_{\parallel}	axial momentum in units of $\mathcal{P}_{\perp 0}$
\mathcal{P}	absolute value of momentum
\mathcal{P}_{\parallel}	axial momentum
\mathcal{P}_{\perp}	transverse momentum
$\mathcal{P}_{\parallel 0}$	initial axial momentum
$\mathcal{P}_{\perp 0}$	initial transverse momentum
Q	quality factor of interaction cavity
R	radius of interaction cavity
R	error in boundary condition
r_L	Larmor radius
S	smoothness of spectrum
T_i	ion temperature
t	time
U_{cath}	accelerating voltage (relative to interaction cavity)
U_{coll}	collector voltage (relative to interaction cavity)
$U_{\text{coll},j}$	voltage of j th collector stage (relative to interaction cavity)
U_{mod}	modulating voltage
\mathbf{v}	velocity
v_{\parallel}	axial velocity
v_{\perp}	transverse velocity
$v_{\parallel 0}$	initial axial velocity
$v_{\perp 0}$	initial transverse velocity
W	energy
\dot{W}	time derivative of energy
W_{tot}	total energy
W_{\parallel}	energy associated with axial motion
x	Cartesian coordinate
y	Cartesian coordinate
z	Cartesian (axial) coordinate
z_{coll}	axial location of collector
z_{out}	axial location of cavity end
z_L	spatial Larmor period
Δz_{ret}	spatial extension of retarding region
α	pitch factor $\beta_{\perp}/\beta_{\parallel}$
$\alpha_{\epsilon}^{\beta}$	corrected pitch factor: $\alpha \rightarrow \alpha_{\epsilon}^{\beta}$ as $\beta_{\perp 0} \rightarrow \beta_{\perp 0}(1 + \epsilon)$

β	absolute value of velocity in units of c
$\beta_{ }$	axial velocity in units of c
$\beta_{ 0}$	initial axial velocity in units of c
β_{\perp}	transverse velocity in units of c
$\beta_{\perp 0}$	initial transverse velocity in units of c
$\beta_{\perp, \text{center}}$	central value of β_{\perp}
$\beta_{\perp, \text{max}}$	maximum value of β_{\perp}
$\beta_{\perp, \text{min}}$	minimum value of β_{\perp}
$\delta\beta_{\perp}$	spread in β_{\perp}
γ	wave number in units of $\beta_{\perp 0}^2 \omega_H / 2\beta_{ 0} c$
γ_{rel}	relativistic factor $(1 - \beta^2)^{-1/2}$
Δ	frequency mismatch
$\Delta_{\epsilon}^{\beta}$	corrected frequency mismatch: $\Delta \rightarrow \Delta_{\epsilon}^{\beta}$ as $\beta_{\perp 0} \rightarrow \beta_{\perp 0}(1 + \epsilon)$
ϵ	relative error in $\beta_{\perp 0}$
ζ	axial coordinate in units of $2\beta_{ 0} c / \beta_{\perp 0}^2 \omega_H$
$\tilde{\zeta}$	transformed axial coordinate in units of $2\beta_{ 0} c / \beta_{\perp 0}^2 \omega_H$
ζ_0	starting point of numerical integration
ζ_1	end point of first numerical integration step
ζ_{out}	axial location of resonator end in units of $2\beta_{ 0} c / \beta_{\perp 0}^2 \omega_H$
η	total efficiency of gyrotron with depressed collector
η_0	total efficiency without depressed collector
η_{coll}	collector efficiency
η_{el}	electron efficiency
η_{\perp}	perpendicular efficiency
ϑ	phase of rotation
ϑ_0	initial phase of rotation
λ	wavelength
μ	length of interaction cavity in units of $\beta_{ } \lambda / \pi \beta_{\perp}^2$
μ_{ϵ}^{β}	corrected cavity length: $\mu \rightarrow \mu_{\epsilon}^{\beta}$ as $\beta_{\perp 0} \rightarrow \beta_{\perp 0}(1 + \epsilon)$
σ	standard deviation
τ_E	confinement time of energy
ξ_j	fraction of total current on j th collector stage
ϕ_{cath}	accelerating voltage in units of $m_e c^2 / e$
ϕ_{coll}	collector voltage in units of $m_e c^2 / e$
χ	eigenvalue of resonating mode
ω	angular frequency
ω_H	electron cyclotron frequency

Chapter 1

Introduction

Fast population growth and economic development are rapidly increasing the world energy demand. The future needs can not be covered in a sustainable way by the present main energy sources. Fossil fuels suffer from pollution problems and limited resources. Conventional nuclear energy is not fully accepted due to waste problems and the risk of reactor accidents. The renewable energy sources (e. g. solar, wind, and biomass) have a low energy density, which makes them rather unsuitable for large-scale base load electricity production. Fusion energy, however, does not suffer from these limitations [1]:

- The fusion reaction takes place between the two heavy isotopes of hydrogen. *Deuterium* can be extracted from water, *tritium* can be produced from lithium, which is abundant. The reaction product, pure helium, is harmless.
- Fusion power plants will be inherently safe.
- The energy content of the fuel is huge. Even though one liter of ordinary water contains only about 0.02 g deuterium, it is enough to yield the energy equal to that obtained from a barrel of oil.

The advantages of fusion are so obvious that worldwide research is carried out on several alternative concepts aiming at the same ultimate goal. In the field of magnetic confinement fusion (Fig. 1.1 explains the basics of magnetic fusion), researchers have reported plasma conditions close to breakeven. Breakeven means that the fusion power equals the power needed for heating and confinement. The next breakthrough is expected to be achieved with the International Thermonuclear Experimental Reactor (ITER). It should be able to create a “burning” plasma, that is, a plasma which sustains the fusion reaction without external power input.

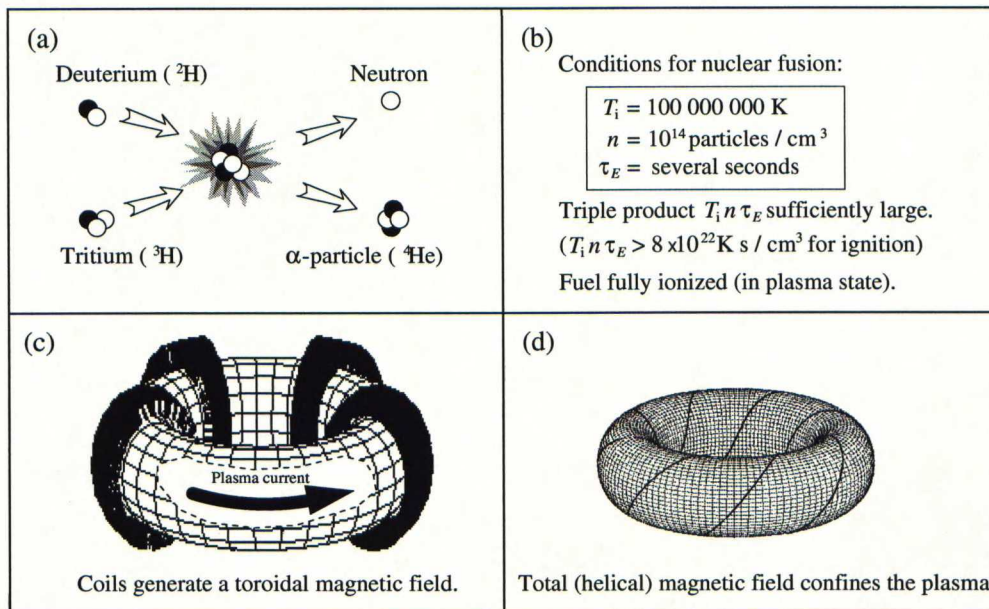


Figure 1.1: (a) The most promising fusion reaction is that occurring between the two heavy isotopes of hydrogen, deuterium and tritium. The nuclei can collide releasing energy and forming an α -particle (helium nucleus) and a neutron. (b) The reaction between deuterium and tritium requires an extremely high temperature T_i at which the fuel is fully ionized—it becomes a plasma that must be confined at density n for a sufficiently long time τ_E [2]. (c) The plasma consists of charged particles and can therefore be confined using magnetic fields (see also Fig. 2.1 on page 17). In a tokamak these fields are produced by coils and a current in the plasma. (d) The coils and the plasma current together generate a helical magnetic field that is suitable for confinement. The charged ions and electrons follow the field lines gyrating about them. [1]

Despite the continuous progress, enormous technological difficulties remain to be solved. In the magnetic fusion, with a plasma confinement device called *tokamak*, there are two important technological questions: First, how to heat the fuel plasma to a temperature of 100 million degrees? Second, how to produce the plasma current that is necessary for confinement? An answer to both problems can possibly be provided by high-power microwaves, which are electromagnetic radiation with frequencies between 1 GHz and 300 GHz [3]. The corresponding wavelengths range from 300 mm to 1 mm, and microwaves are also called millimeter waves. In this context high power means an average power from 10 kW to several MW for a continuous wave, and

peak powers from a few MW up to GW range for shorter pulses.

A fusion plasma can be heated to the desired temperature by irradiating it with microwaves or by injecting energetic neutral particle beams into the reactor. Microwave heating technologies utilize *resonances*: the wave frequency is chosen to correspond to some characteristic frequency of the plasma. Since fusion plasmas are not uniform, the resonance (which implies very strong interaction with the plasma particles) occurs only at certain positions; elsewhere the wave propagates almost freely. The wave energy is therefore delivered to the plasma particles with a high efficiency and a good spatial accuracy. Neutral beam particles travel into the reactor across the confining magnetic field until they are ionized in collisions with the high temperature plasma. Ionization makes the particles charged, they become trapped by the magnetic field, and give their energy to the plasma through collisions with the plasma particles.

Compared to neutral beams, the microwaves have many advantages in heating a fusion plasma. First, microwave heating provides various interaction mechanisms at different frequencies: the ion cyclotron frequency regime (10–100 MHz), the lower hybrid frequency regime (1–10 GHz), and the electron cyclotron frequency regime (100–300 GHz). Thus there is a lot of freedom to optimize the heating; it can e. g. be targeted to electrons or ions after desire. Secondly, wave power can easily be delivered from sources located round a corner and thus shielded from neutrons escaping from the reactor. [4] In many respects the most advantageous microwave devices are electron cyclotron wave (ECW) sources. They can be used remotely, whereas lower hybrid and ion cyclotron waves require an intimate contact with the hot plasma edge. Also, the ECW power is transmitted through a small area in comparison to large and expensive lower hybrid and ion cyclotron wave antennas. Furthermore, the interaction between the ECW's and the edge plasma is only weak, so that both remain practically undisturbed when the wave travels towards the center of the plasma across the edge. [5, 6]

In addition to heating, microwaves have been established as the standard means to drive current inside the plasma. Microwaves also have a wide range of applications in plasma diagnostics, although the measurements are technically very demanding [7]. Furthermore, intense microwaves are being developed to be applied to controlling the radial profile of the plasma current. Finally, the possibility of manipulating the "fusion ash" is currently under investigation: the helium nuclei could be cooled down using microwaves before extracting them from the plasma. [4]

Besides fusion research, intense microwave sources find applications in particle physics, radar technology, and various industrial processes. High-power microwave sources are needed as drivers to achieve 1 TeV energy in

an electron-positron collider [8]. Atmospheric sensing takes advantage of high-power microwave technology [9]. In this field the applications include observing the structure of clouds and turbulence of clear air, as well as rapid humidity and impurity measurements. Many tasks in material processing (e. g. sintering and brazing of advanced structural and functional ceramics, surface hardening or dielectric coating of metals and alloys, polymerization and burning of pastes in semiconductor thick-film technologies) and plasma chemistry are also carried out using microwave sources [10].

In the high-power range, only vacuum electronics can provide competitive sources for microwave generation. Today there exist many different electron tube constructions for this purpose. The differences between various tubes are briefly discussed in the next chapter. A *gyrotron*, also called *electron cyclotron maser (ECM)*, is one of these tubes. The typical frequency range of gyrotrons is 20–200 GHz.

All the applications mentioned above are particularly well-suited for gyrotrons. In the frequency range of interest, their output power is superior to other sources [11]. Nevertheless, fusion technology is continuously driving the development of gyrotrons further [12]. The present gyrotrons are capable of producing up to 1 MW power at 110–170 GHz in long pulse or continuous wave operation. For future electron cyclotron heating systems to be cost-effective, more power per tube will be needed [13]. For example, the heating system designed for ITER requires at least 25 MW of continuous-wave radio-frequency power at frequencies close to 170 GHz [14]. One way to raise the output power is to improve the overall efficiency of the tube.

The most serious power loss in a gyrotron is the residual energy of electrons. They hit the collector at a high velocity and heat it. A significant increase in efficiency can be achieved by using a *depressed potential collector*, which decelerates the electrons before the impact. For multi-megawatt systems this can mean remarkable savings in investments as well as in operation costs. Also technological benefits arise due to the reduced heat load and x-ray generation at the collector surface. There are still some problems to be solved in order to improve the efficiency of depressed collectors. In this work the answers to the following questions are sought:

- For a depressed collector to work efficiently, the electron residual energies must be known. Is there a risk that this knowledge is lost due to chaotic electron trajectories in the resonator? In particular, can electrons behave chaotically during high-efficiency operation of a gyrotron?
- The depressed collector may reflect some incoming electrons. What is the influence of the reflected electrons to the efficiency, and how high retarding potentials can be safely applied?

The questions are investigated by computer modeling, supplemented by theoretical calculations.

This thesis is organized as follows. In Chapter 2 the reader is given an introduction to gyrotrons. To provide enough background for the later work, some areas of the existing theory are discussed in detail. Because depressed collectors play a central role, they are introduced separately in Chapter 3. In Chapter 4, the results related to chaos studies are reported, while the effects of electron trapping are investigated in Chapter 5. Conclusions are drawn and recommendations given in Chapter 6.

Chapter 2

Gyrotrons

2.1 Operating principle

Gyrotron is a microwave tube designed to produce coherent radio-frequency waves of high power and high intensity. The waves are created by electrons which execute helical motion (see Fig. 2.1) in a strong magnetic field. Because the electrons are bunched in phase due to relativistic effects (see Section 2.3.2), the radiation is coherent. The wave energy is extracted from electrons which have been accelerated with a magnetron injection gun (MIG). The wave is generated in a specially designed interaction cavity (resonator) which can sustain oscillations on the desired frequency. In modern gyrotrons the specific mode generated in the resonator is converted by a mode converter into a Gaussian beam which is directed by means of special mirrors out of the gyrotron through a diamond window. The decelerated electron beam, instead, is separated from the wave and dumped onto a collector where its residual energy is dissipated. For a schematic picture of a gyrotron, see Fig. 3.1 on page 25.

This chapter is devoted to introducing the physics of wave generation and suitable models for it. Major emphasis is given to the subjects that are most essential for the work reported in Chapters 4 and 5.

2.2 Electron gun

The operation of electron guns used in gyrotrons is based on thermionic emission of electrons from a cathode material [15]. The current is limited by the cathode temperature; a fact that provides a possibility to control the current and guarantees operating conditions for which a mature theory exists today [16]. The resonator acts as an anode and attracts the beam towards

it. The path of electrons is, however, limited by the magnetic field such that they will not hit the cavity surface. Additional control over the beam properties can be achieved by adjusting the accelerating electric field in the vicinity of the cathode with a modulating anode.

Gyrotrons typically exhibit cylindrical symmetry which immediately requires the electron beam also to be circular. Since the electric field varies radially in the resonator, and since a strong field is preferable to enhance the interaction, there is an optimal radius at which the electrons should be emitted. The cathode therefore has only a ring that emits electrons as an annular beam. [16]

For most of our purposes, it is sufficient to know the accelerating voltage U_{cath} of the MIG and the pitch factor α , the ratio between perpendicular and parallel velocity of the electron beam. In practice, however, there may be significant spread in the electron velocities—a fact that strongly reduces the gyrotron efficiency [17]. This aspect will be touched in the present study, too (see Section 5.4.2).

2.3 Interaction between electrons and the HF field

2.3.1 Electron motion in an electromagnetic field

The motion of an electron in an electromagnetic field is governed by the equation

$$\frac{d\mathbf{p}}{dt} = -e(\mathbf{E} + \mathbf{v} \times \mathbf{B}), \quad (2.1)$$

where $-e$ is the charge of electron, \mathbf{p} its momentum and \mathbf{v} velocity, \mathbf{E} and \mathbf{B} the electric and magnetic field, respectively. It is often convenient to divide the velocity into two components, one of which ($v_{\parallel} = \beta_{\parallel}c$) is parallel to the magnetic field and the other one ($v_{\perp} = \beta_{\perp}c$) perpendicular to it. In the *guiding center approximation* valid for sufficiently homogenous fields the particle motion consists of the motion of the *guiding center* along a magnetic field line and the gyration around the guiding center at the *electron cyclotron frequency*

$$\omega_H = \frac{eB}{\gamma_{\text{rel}}m_e}. \quad (2.2)$$

Here m_e is the electron rest mass and $\gamma_{\text{rel}} = (1 - \beta_{\parallel}^2 - \beta_{\perp}^2)^{-1/2}$ the relativistic mass factor, which can also be expressed in terms of the accelerating potential difference U_{cath} :

$$\gamma_{\text{rel}} = 1 + \frac{eU_{\text{cath}}}{m_e c^2} = 1 + \frac{U_{\text{cath}}}{511 \text{ kV}}. \quad (2.3)$$

The radius of the gyro-motion is called the *Larmor radius* and is given by

$$r_L = \frac{mv_{\perp}}{eB} = \frac{\mathcal{P}_{\perp}}{eB}, \quad (2.4)$$

where \mathcal{P}_{\perp} is the momentum component perpendicular to the magnetic field. Fig. 2.1 illustrates electron orbits in a uniform field.

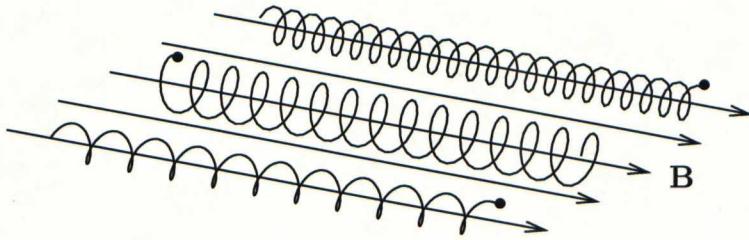


Figure 2.1: *Electron orbits in a uniform magnetic field \mathbf{B} .*

2.3.2 Bunching mechanism in gyrotrons

We can find the rate of change of the energy of an electron by taking the scalar product of (2.1) with \mathbf{v} :

$$\frac{dW}{dt} = \frac{d\mathbf{p}}{dt} \cdot \mathbf{v} = -e\mathbf{E} \cdot \mathbf{v}, \quad (2.5)$$

since $(\mathbf{v} \times \mathbf{B}) \perp \mathbf{v}$. We conclude that those electrons which have a velocity component in the direction of \mathbf{E} are decelerated ($\dot{W} < 0$), and those with a velocity component opposite to \mathbf{E} are accelerated ($\dot{W} > 0$).

Essential for the operation of a gyrotron is the energy dependence of the cyclotron frequency, see Eq. (2.2). The gyration slows down due to the relativistic mass increase with energy. It is also worth noting that the Larmor radius r_L increases with energy.

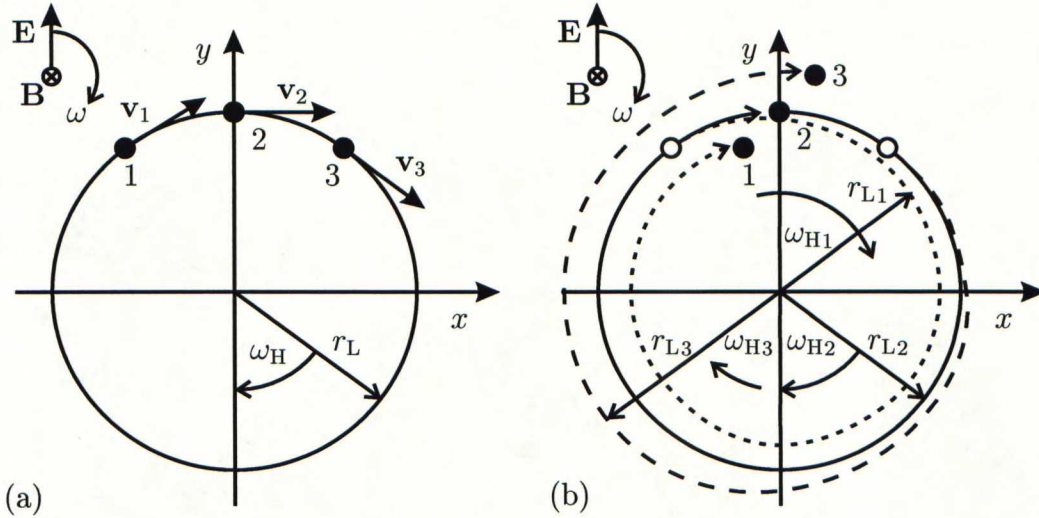


Figure 2.2: Illustration of the azimuthal bunching mechanism in a gyrotron. Due to the different phases with respect to the rotating electric field, the gyrating electrons may gain energy or transfer it to the field. In the situation shown in (a), electron 1 loses energy and electron 3 gains it, while the field does no work on electron 2 which moves perpendicularly to the field. In (b), the resulting bunching (exaggerated) after one field period is shown. The effect is due to the relativistic dependence of cyclotron frequency on electron energy.

The behavior of a beamlet of electrons can be explained using the following simplified model illustrated in Fig. 2.2. Let us consider three electrons (labeled 1, 2 and 3) having an equal initial energy ($|\mathbf{v}_1| = |\mathbf{v}_2| = |\mathbf{v}_3|$) and gyrating about a common guiding center in a uniform static magnetic field. Fig. 2.2 (a) shows the phases of rotation and the electron velocities when we start following them. The Larmor radii of the electrons with same energy are equal. The RF field present in the interaction cavity is described by a rotating electric field which we assume to be uniform over the region of interest. Furthermore, let the angular frequency of rotation (ω) be equal to the electron cyclotron frequency ω_H .

Due to the different angles between velocity and electric field vector the electron energies do not change similarly. We can summarize the effects of Eqs. (2.2), (2.4) and (2.5) as follows:

1. For electron 1 the scalar product $\mathbf{E} \cdot \mathbf{v} > 0$, consequently, it is decelerated. This leads to an increase in the cyclotron frequency and a decrease in the Larmor radius.
2. Electron 2 is moving perpendicularly to the electric field and does there-

fore not experience any change in energy. Its cyclotron frequency and Larmor radius remain constant, and it stays in phase with the rotating field.

3. Opposite to the first electron, the third one is accelerated. This slows down the gyration and increases the Larmor radius.

After one field period [see Fig. 2.2 (b)] the electric field again points as in (a), but the electrons have been bunched around the positive y -axis. [18]

2.3.3 Energy exchange between electrons and the HF field

In the simple model of the previous section we found that one electron was accelerated while another was decelerated. The net energy exchange between electrons and the high-frequency field turned out to be zero. To make the gyrotron work as an amplifier of the wave, most electrons should be decelerated by the electric field. This situation can be achieved by setting the frequency ω slightly larger than ω_H . Then the electron bunch will slip behind the wave and end up in the decelerating phase of rotation. [19]

2.3.4 Dispersion diagram of a gyrotron

The operation of different microwave tubes can be compactly presented using their *dispersion diagrams*. They show the dispersion relation of the waveguide mode

$$\omega^2 = k_{\parallel}^2 c^2 + k_{\perp}^2 c^2 \quad (2.6)$$

together with the beam-wave resonance line

$$\omega - k_{\parallel} v_{\parallel} \approx \omega_H. \quad (2.7)$$

Here ω is the frequency of the wave, ω_H the cyclotron frequency, and k_{\parallel} and k_{\perp} are the wave numbers in the axial and radial direction, respectively. The axial velocity of the beam is v_{\parallel} . The gyrotron resonance occurs where the two frequencies of Eqs. (2.6) and (2.7) are equal. In fast-wave devices such as the gyrotron, the Doppler-shift term $k_{\parallel} v_{\parallel}$ is small, and the resonance condition reads:

$$\omega \approx \omega_H. \quad (2.8)$$

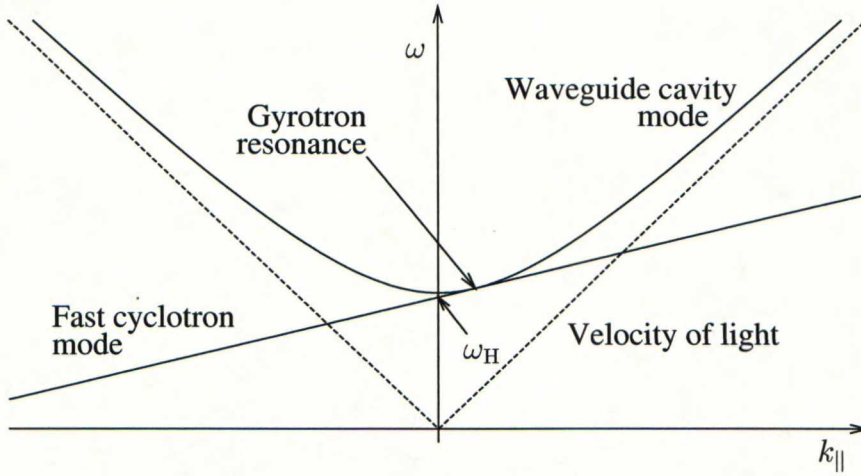


Figure 2.3: *The dispersion diagram of a gyrotron operating at the fundamental frequency [20]. Gyrotron is a forward-wave oscillator, that is, the resonance takes place at a positive value of $k_{||}$. Moreover, the gyrotron is classified as a fast-wave device, since the phase velocity v_{ph} of the electromagnetic wave exceeds c . The dashed line corresponds to the velocity of light, $\omega = k_{||}c$.*

The dispersion diagram for the gyrotron is shown in Fig. 2.3. [20] Other microwave tubes—klystrons, traveling-wave tubes (TWT), backward-wave oscillators (BWO), etc.—have different dispersion diagrams. A major theoretical difference between the gyrotron and slow-wave devices (e. g. TWT, BWO) is in the phase velocity v_{ph} of the electromagnetic wave. In fast-wave devices $v_{ph} > c$, whereas slow-wave devices utilize a wave with $v_{ph} < c$ [21].

2.3.5 Gyrotron equations

Self-consistent equations

In this work the evolution of electron energies during the interaction is of major interest, and equations describing it are needed. A suitable model has been presented in [22]. The model is based on the solution of the complete three-dimensional wave equation in a cylindrical cavity, the effect of the electron current having been taken into account. The high-frequency field is supposed to oscillate in time as $\exp(-i\omega t)$, and its amplitude is a function of all three coordinates. The field can be expressed as a product of three factors, each of which is a function of only one coordinate. We are interested in the

dependence on the axial coordinate, given by a function f . The information about the shape of the field in other directions is included in the parameter I introduced below.

The two transverse components of the physical momentum \mathcal{P} are denoted by a normalized complex quantity p , for which $|p| = \mathcal{P}_\perp / \mathcal{P}_{\perp 0}$. The axial coordinate z is normalized according to $\zeta = (\beta_{\perp 0}^2 \omega_H / 2\beta_{\parallel 0} c) z$, where $\beta_{\perp 0} = v_{\perp 0} / c$ and $\beta_{\parallel 0} = v_{\parallel 0} / c$ are the normalized transverse and parallel velocities of the electron at the entrance to the cavity, respectively. Using this notation and restricting ourselves to operation at the fundamental frequency, the motion of a electrons and the electromagnetic field in the resonator can be described by the equations

$$\frac{dp}{d\zeta} = -ip(\Delta + |p|^2 - 1) + if, \quad (2.9)$$

$$\frac{df}{d\zeta} = -\gamma^2 f + I \times \frac{1}{2\pi} \int_0^{2\pi} p d\vartheta_0. \quad (2.10)$$

We use an initial condition $p(0) = \exp(i\vartheta_0)$, where $\vartheta_0 \in [0, 2\pi]$, and boundary conditions $f'(0) = i\gamma f(0)$, $f'(\zeta_{\text{out}}) = -i\gamma f(\zeta_{\text{out}})$. The normalized wave number γ can be written as

$$\gamma = \frac{2\beta_{\parallel} c}{\beta_{\perp}^2 \omega_H} \sqrt{\frac{\omega^2}{c^2} - \frac{\chi(\zeta)^2}{R(\zeta)^2}},$$

the functions χ and R being the eigenvalue of the resonating mode and the radius of the interaction cavity, respectively. The frequency mismatch $\Delta = 2(\omega - \omega_H) / \beta_{\perp 0}^2 \omega$ brings about the effect of the magnetic field via the cyclotron frequency ω_H . I is the normalized current; for its explicit expression, see, e. g., [22].

The boundary conditions for (2.10) have been written for a plane wave. At the input ($\zeta = 0$) the wave is evanescent ($\gamma^2 < 0$), whereas it is propagating ($\gamma^2 > 0$) at the output ($\zeta = \zeta_{\text{out}}$). [23]

The system (2.9)–(2.10) is an initial value problem for p , but also an eigenvalue problem in ω , since both boundary conditions for f cannot be satisfied simultaneously for arbitrary ω . The method chosen for the numerical solution will be presented in Section 4.5.1.

Cold-cavity approximation

In the so-called *cold-cavity approximation* it is assumed that only the geometry of the interaction cavity—not the electrons in it—affects the high-frequency field profile. This assumption decouples the equations:

$$\frac{dp}{d\zeta} = -ip(\Delta + |p|^2 - 1) + iFf, \quad (2.11)$$

$$\frac{df}{d\zeta} = -\gamma^2 f. \quad (2.12)$$

The frequency is treated as a complex quantity $\omega = 2\pi F_\omega(1 + i/Q)^{1/2}$, where F_ω is the eigenfrequency and Q is called the quality factor of the cavity. The imaginary part of the frequency accounts for wave damping due to radiation out of the cavity. The expression for the coupling factor F between the electron beam and the high-frequency field is given, e. g., in [24].

Even after finding the values of F_ω and Q to match the complex boundary conditions for the high-frequency field, the solution $f(\zeta)$ of Eq. (2.12) can be multiplied by an arbitrary non-zero complex constant. This degree of freedom is used to normalize f so that

$$\max_{\zeta \in [0, \zeta_{\text{out}}]} |f(\zeta)| = 1$$

and

$$f(0) \propto e^{i\gamma(\zeta=0)}.$$

Within the cold-cavity model a Gaussian field profile

$$f(\zeta) = \exp \left[- \left(\frac{2\zeta}{\mu} - \sqrt{3} \right)^2 \right] \quad (2.13)$$

is often used, which is a reasonable approximation for high- Q resonators. Here $\mu = \pi\beta_\perp^2 L / \beta_\parallel \lambda$ is the dimensionless length of the interaction cavity whose physical length is L . In this approximation the axial field profile is taken to be symmetric about the center of the cavity, which yields $\zeta_{\text{out}} = \sqrt{3}\mu$.

When calculated self-consistently, the field amplitude is fully determined by Eqs. (2.9)–(2.10). In some contexts, however, also this field is normalized as stated above. For example, the quality factor Q can be calculated using

the normalized self-consistent solution according to the formula

$$Q = \frac{1}{I\eta_{\perp}} \frac{8\beta_{\parallel}^2}{\beta_{\perp}^4} \left(\frac{\omega}{\omega_H} \right)^2 \int_0^{\zeta_{\text{out}}} |f|^2 d\zeta. \quad (2.14)$$

Another useful relation between the quantities of the self-consistent model and the cold-cavity approximation can be written for I and F with the help of perpendicular efficiency introduced in Section 2.3.6:

$$F^2 = \frac{4\mu}{5\pi} \eta_{\perp} I, \quad (2.15)$$

Eq. (2.15) is, in fact, a representation of the energy balance of the gyrotron. [25]

2.3.6 Efficiency of a gyrotron

The *perpendicular efficiency* η_{\perp} is calculated by averaging the squared orbital momentum at the cavity output over all electrons:

$$\eta_{\perp} = 1 - \frac{1}{2\pi} \int_0^{2\pi} |p(\zeta_{\text{out}})|^2 d\vartheta_0. \quad (2.16)$$

However, the electrons give only their transverse energy to the wave; the longitudinal momentum remains unchanged during the interaction. To obtain the total electron efficiency η_{el} , the perpendicular efficiency must be multiplied by the fraction of perpendicular energy in the total kinetic energy:

$$\eta_{\text{el}} = \frac{\alpha^2}{1 + \alpha^2} \eta_{\perp}, \quad (2.17)$$

where $\alpha = \beta_{\perp}/\beta_{\parallel}$ is the pitch factor of the electrons.

Chapter 3

Depressed Collectors

3.1 General about collectors in gyrotrons

Depressed collectors seem to be an attractive way to achieve a major improvement in gyrotron overall efficiency. In experiments, efficiency enhancements such as 30 % \rightarrow 50 % [26], 31 % \rightarrow 51 % [27] and 40 % \rightarrow 65 % [28] using a single-stage depressed collector have been reported. The advantages include not only the lower power consumption using less costly power supplies, but also the reduced heating and x-ray generation on the collector surface [27, 29]. In gyrotrons with axial output, the collector also acts as a waveguide, which sets certain requirements for its shape and surface quality. These requirements combined with the high heat load make the design of a collector for a high-power gyrotron complicated, and it is often seen desirable to separate the wave from the electron beam. [30] Here the potential depression provides an alternative solution. For a large RF power system, the use of depressed collectors could result in savings of hundreds of millions of dollars in investments as well as in operating costs, see [31, 32].

In this chapter, the principle and main design issues for depressed collectors are presented. A specific problem related to the subject—electron reflection and trapping due to the retarding potential—is studied in more detail in Chapter 5.

3.2 Effect of a depressed collector on efficiency

Gyrotron interaction is based on the fact that the high-frequency field gains energy from the rotational motion of electrons. The axial energy of the electrons, on the other hand, remains unchanged during the interaction; all electrons in the spent beam therefore have at least the amount of energy cor-

responding to the initial longitudinal motion. In a gyrotron without collector potential depression, all residual energy is deposited on the collector surface, causing a demand for efficient cooling. A depressed collector, instead, produces an electric field which decelerates the incoming electrons before they hit the collector. A part of the kinetic energy of the spent beam is in this way transformed back into electric energy. For a schematic picture of a gyrotron with a depressed collector, see Fig. 3.1.

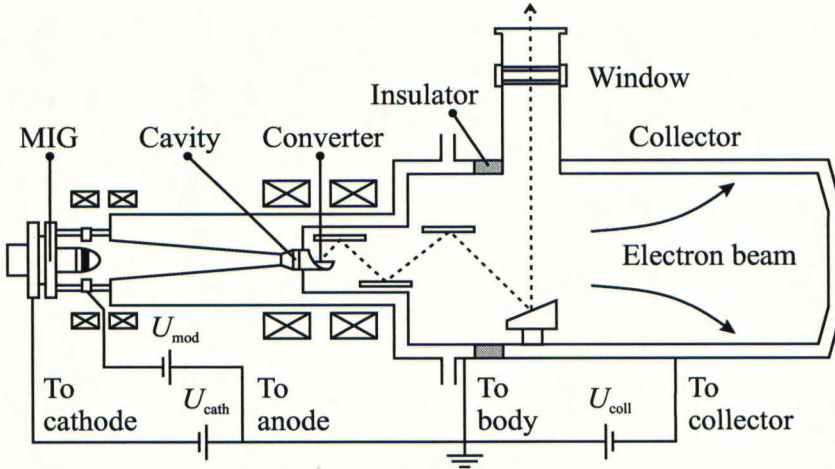


Figure 3.1: A schematic picture of a gyrotron with a single-stage depressed collector.

A depressed collector may have several collector stages (multi-stage depressed collector, MDC) or only one (single-stage depressed collector, SDC). The collector stages are insulated from the grounded body of the device and from each other so that a voltage between them can be applied. The interaction cavity (anode) is taken to be at zero potential whereas the absolute values of the cathode and the n collector potentials are denoted by U_{cath} and $U_{coll,j}$ ($j = 1, \dots, n$), respectively. Using these, the total efficiency η can be written as the ratio of RF output power $P_{RF} = \eta_0 I_0 U_{cath}$ and the power consumption $P = \sum_{j=1}^n I_j (U_{cath} - U_{coll,j})$ to obtain

$$\eta = \frac{\eta_0}{1 - \sum_{j=1}^n \xi_j U_{coll,j} / U_{cath}}, \quad (3.1)$$

where η_0 is the total efficiency without a depressed collector and ξ_j ($j = 1, \dots, n$) are the relative fractions of the total current I_0 on each collector

stage, including possible body current. In particular, for a gyrotron with a SDC ($n = 1$) in the potential $-U_{\text{coll}}$ we find

$$\eta = \frac{U_{\text{cath}}}{U_{\text{cath}} - U_{\text{coll}}} \eta_0. \quad (3.2)$$

Let us still define another related concept. The quality of a depressed collector is described by the *collector efficiency* [27]

$$\eta_{\text{coll}} = \frac{P_{\text{coll}}}{P_{\text{b}} - P_{\text{RF}}}, \quad (3.3)$$

where P_{coll} is the power recovered into the circuit by the collector, and $P_{\text{b}} = I_0 U_{\text{cath}}$ is the initial beam power. Equivalently [32],

$$\eta = \frac{\eta_0}{1 - \eta_{\text{coll}}(1 - \eta_0)}.$$

3.3 Design issues

3.3.1 Conversion from rotational to axial energy

The retarding electric field in the depressed collector is predominantly axial and cannot therefore be used to recover energy associated with the rotational motion. Since typically 70–80 % of the beam energy is rotational, a conversion mechanism is needed. An obvious choice is to let the guiding magnetic field diverge between the resonator and the collector, thus making the rotation slow down and the corresponding kinetic energy turn into axial motion within adiabatic approximation. Any desired level of energy conversion in this way seems possible. [32]

In practice, the adiabaticity cannot always be sustained to large decompression factors without making the spatial dimensions available for the process impractically large. The Larmor period $z_{\text{L}} = \mathcal{P}_{\parallel}/eB$ increases during the decompression so that the magnetic field strength is allowed to decrease slower and slower. On the other hand, the Larmor radius $r_{\text{L}} = \mathcal{P}_{\perp}/eB$ increases (known that $\mathcal{P}_{\perp} \propto B^{1/2}$); thus more space is needed in the radial direction also. The axial and rotational momentum components were here denoted by \mathcal{P}_{\parallel} and \mathcal{P}_{\perp} , respectively. [32]

When one is forced to apply a non-adiabatic change of the magnetic field, it is preferable to implement in the following way: adiabatic decompression is continued to a prescribed value of B , and then a step-like non-adiabatic

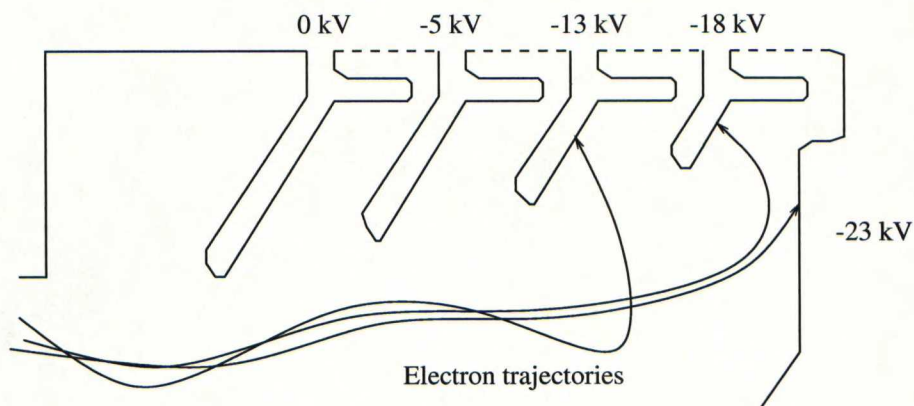


Figure 3.2: An example of multi-stage depressed collector geometry [36].

transition to zero field is applied. The remaining transverse momentum can in this fashion be limited to an acceptable value. [32] In fact, an advantage of a controlled non-adiabatic step is its ability to spread the electrons more evenly at the collector surface and thus prevent undesired hot spots from occurring [33].

3.3.2 Collector geometry

In a multi-stage depressed collector, the shape of the collector plates at different potentials is a key issue: the beam electrons must be separated into energy groups using the combination of the prevailing magnetic field and the electric field created by the collector. An inhomogeneity of the magnetic field can be used in separation: the degree of adiabaticity of an electron's motion depends on its energy and, consequently, electrons of different energy gain different amounts of transverse motion. [34, 35] In some studies [29, 33] the electron trajectories are calculated using an *effective potential*, which simultaneously takes into account both the electric and magnetic field.

In addition to the true *primary* electrons approaching the collector after the interaction, the effective potential model can be used to follow backscattered primary and *secondary* electrons, that is, electrons emitted by the surface atoms as a result of the impact. These electrons should be made return back to the emitting surface, which in practice means that the primary electrons should hit the back side of the plate. Their axial motion must therefore be reversed before the impact. [31] An example of a suggested collector geometry is shown in Fig. 3.2.

3.3.3 Surface materials

The above-mentioned generation of secondary electrons is strongly dependent on the surface material. In a traveling-wave-tube operated with a MDC, an improvement factor of 1.10–1.15 for overall and collector efficiencies has been reported when copper electrodes were replaced by isotropic graphite electrodes [37]. This improvement is due to the difference in the overall backscatter coefficients of these materials. For example, the value of this coefficient over the energy range 100–300 keV of the impinging electrons is 0.3 for copper while it is 0.05 for graphite. Instead of making a solid graphite electrode, it is possible to coat a copper electrode with graphite. [31] Regardless of the choice of surface material, the need for optimal shaping of the collector plates is evident.

3.4 Current status of development and future prospects

The experiments reported in [26] were the first long-pulse tests on a gyrotron with a depressed collector [38]. The usage of single-stage depressed collectors in gyrotrons has proved to be relatively unproblematic [27]. As far as we know, gyrotrons have not been operated with multi-stage depressed collectors. However, MDC's have been established in use in other microwave tubes, and it seems probable that they will also be used to improve the gyrotron efficiency in the future. Theoretical work towards their implementation is well on the way.

Chapter 4

Electron Residual Energies in Gyrotrons

4.1 General

During the past few years, several authors have been concerned by chaotic electron trajectories developing in gyrotrons [39, 40, 41]. Indeed, knowledge about electron residual energies is vital when designing depressed collectors to improve the overall efficiency of a gyrotron. Chaos, when present in the interaction cavity, would make the energies of outcoming electrons unpredictable and, consequently, an efficient depressed collector would be impossible to construct. In this chapter the risk of chaos in the most favorable operating regimes of a gyrotron is studied.

4.2 Definition of chaos

A *dynamical system* can be described as a system of N first-order differential equations

$$\frac{dx_j}{dt} = g_j(x_1, \dots, x_N, r), \quad j = 1, \dots, N, \quad (4.1)$$

where t is the independent variable (often time) and the $x_j(t)$ are dynamical quantities whose evolution is governed by (4.1), starting from specified initial conditions $x_j(0)$, $j = 1, \dots, N$. The functions g_j are nonlinear, and they can be characterized by one or more parameters r . [42] A system of the above type is called *autonomous*—not explicitly dependent on t [43].

Chaos can be defined in many different ways, some of which are more strict than others. For our purposes the most suitable concept is *determin-*

istic chaos, which means irregular behavior of dynamical systems having a strictly deterministic evolution in time and no sources of noise or external stochasticity. This irregularity manifests itself as an extremely sensitive dependence on the initial conditions—a fundamental feature that has been taken as a part of the mathematical definition of chaos also; see, e. g. [44].

4.3 Possibility of chaotic electron trajectories in gyrotrons

The gyrotron equation (2.11) can be written as an autonomous system of three ordinary differential equations. The three unknown functions will then be the real and imaginary part of the transverse momentum p and the independent variable ζ (whose derivative is identically 1). It is known from the theory of differential equations that an autonomous dynamical system of at least three equations *may* have chaotic solutions [45]. On the other hand, *there is no guarantee* for this kind of behavior to occur.

In [39] it was suggested that the relativistic increase of electron mass would tend to prevent chaos from developing in gyrotrons. On the other hand, it was shown in [40] that permanently chaotic electron trajectories cannot exist in a resonator with a high quality factor, while the problem for low-quality resonators remains open.

4.4 Numerical evidence about chaos

Electron energy spectra after gyrotron interaction are studied in detail in Section 4.5. However, a specific example is presented here as a motivation for the calculations that will follow.

In Fig. 4.1 are shown the numerically calculated absolute values of the transverse momenta of electrons at the interaction cavity end for different initial phases of rotation. We see that for certain initial conditions the solution is very sensitive to small changes in them. A closer look on the sharp peak at about 30 degrees (see Fig. 4.2) reveals that there is even more sensitivity than can be seen at a first glance. The shape seen in Fig. 4.1 repeats in a small scale. There is an obvious analogy to *fractals*, that is, sets which exhibit self-similarity under magnification [44]. Even though the self-similarity in this example does not continue if we look at the spectrum still closer, it can be regarded as a trace of transient chaos prevailing in the resonator. Be the chaos permanent or transient, due to it the quality of energy spectrum will anyway deteriorate, and any sign about chaos must therefore be taken seriously.

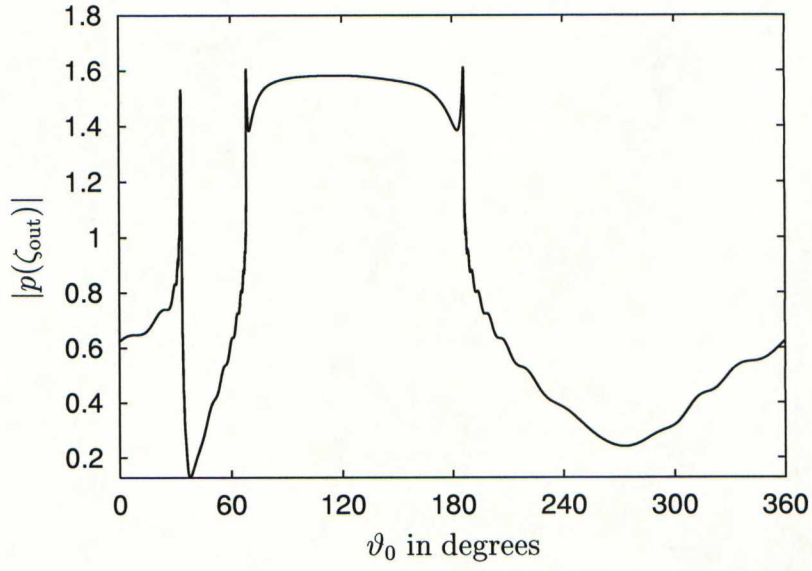


Figure 4.1: *The final electron momenta as a function of the initial phase ($\Delta = 0.50, F = 0.125$).*

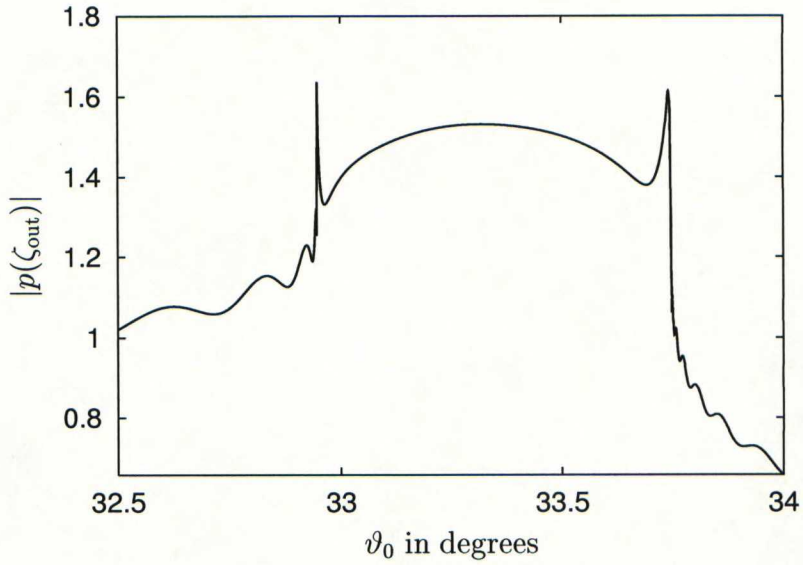


Figure 4.2: *The same spectrum as in Fig. 4.1 but restricted to a narrow range around the single peak.*

4.5 Dependence of electron residual energy on initial conditions

4.5.1 Numerical codes

General about the codes

To solve Eqs. (2.9)–(2.12) numerically, three computer programs were written. The cold-cavity approximation has been used in most computations—it is not only simpler to program but also significantly cheaper to run on computers. For this, separate routines are used for finding the high-frequency field profile and the electron trajectories under the influence of this field. In the self-consistent calculation both tasks are to be solved simultaneously, which was also done as a demonstration and an important check for the results obtained in the cold-cavity approximation.

Solution of the field profile in the cold-cavity approximation

The second-order differential equation (2.12) for the high-frequency field can not be in the usual manner discretized and represented as a linear system of equations for function values at nodes. This complication arises from the form of boundary conditions in which both the value of the function and its derivative are involved. An iterative method of solution (see the flow chart, Fig. A.2 in Appendix A) has therefore been used. The differential equation is treated as an initial value problem with ζ representing time and integrated using fourth-order Runge–Kutta method. The function value and its derivative at the right boundary are then compared to the corresponding boundary condition. A simple minimization routine was written, which changes the frequency F_ω and the quality factor Q to find the minimum of

$$R = |f(\zeta_{\text{out}}) + i\gamma f'(\zeta_{\text{out}})|. \quad (4.2)$$

A feasible initial guess for F_ω and Q is needed to make the iteration converge. Some authors [7, 46] who have dealt with the same problem reformulated the minimization task for numerical calculations, which has not been done in this work. Previously obtained results can still be reproduced. Fig. 4.3 shows the functions that characterize the cavity and Fig. 4.4 the resulting field profile.

Solution of electron motion in the cold-cavity approximation

The evolution of electron momenta during the gyrotron interaction is straightforward to solve when the field profile is known. The same integration routine

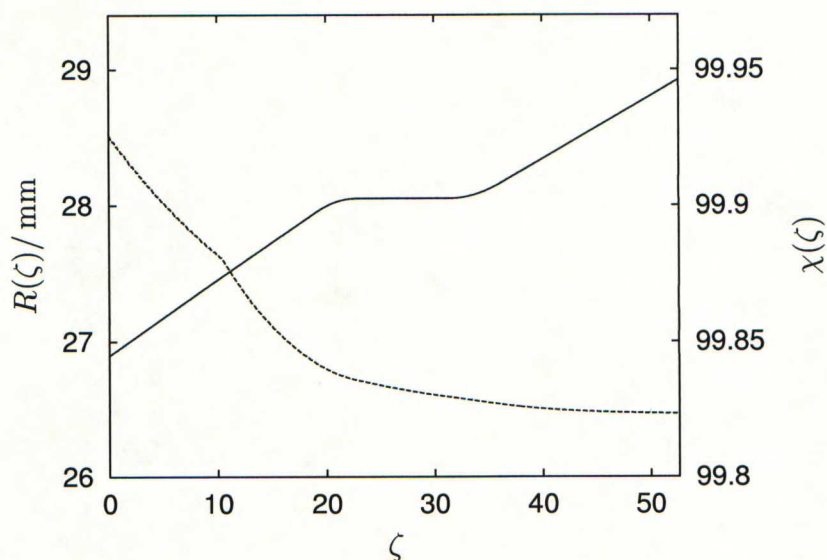


Figure 4.3: The functions $R(\zeta)$ (solid) and $\chi(\zeta)$ (dashed) which describe the interaction cavity. Note the scales: $R(\zeta)$ and $\chi(\zeta)$ change only little. In other words, the gyrotron is operated very close to the cut-off of the wave.

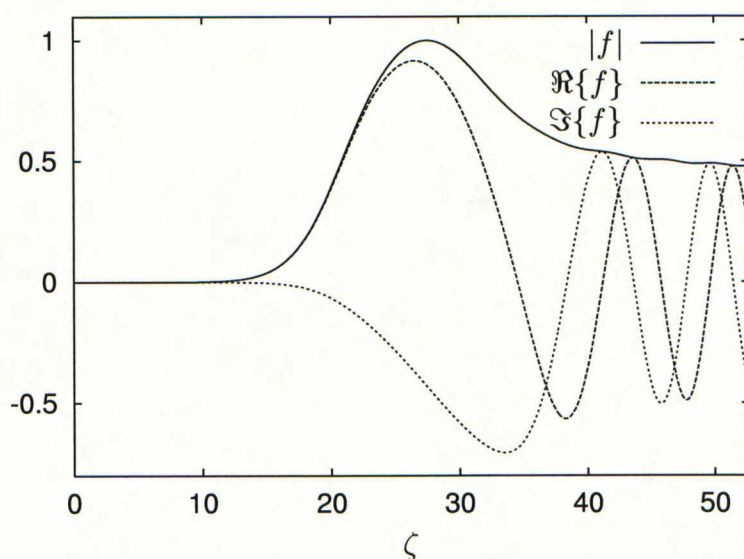


Figure 4.4: The field profile in the cold-cavity approximation.

as in calculation of the field, fourth order Runge–Kutta, was used. After assigning the electrons their initial momenta $p_0 = \exp(i\vartheta_0)$, the trajectories were obtained independently from each other, and the absolute values of the final transverse momenta were recorded. Fig. 4.7 on page 37 shows these results for some parameter combinations. The flow chart for the routine performing the integration for one electron is shown in Fig. A.1 in Appendix A. For the purposes of later work, the routine was made capable of integrating the equation backwards also.

To check the validity of the cold-cavity approximation, some cases were solved in parallel with the self-consistent method. The electron energy spectra obtained for a single combination of parameter values ($\Delta = 0.52$ and $F = 0.098$ or, equivalently, $I = 0.004$) are shown in Fig. 4.5. The striking phase shift between the solutions is not serious—in practice the input phases are outside control in any case. More important is the fact that the correct shape of the spectrum can be found using the cold-cavity approximation. This, of course, also yields the correct perpendicular efficiency. Later we can see that this particular case is not an exception but the spectra in general coincide very well.

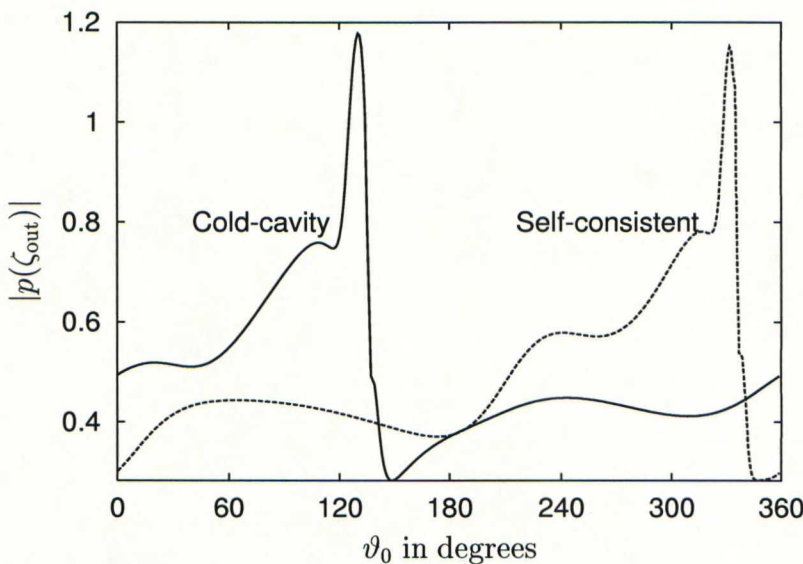


Figure 4.5: *Electron momenta at the cavity end as a function of the input phase calculated in the cold-cavity approximation and self-consistently. Here $\Delta = 0.52$. The self-consistent solution is for $I = 0.004$, for which $\eta_{\perp} = 0.734$; consequently, $F = 0.098$ in the cold-cavity calculation according to (2.15).*

Self-consistent solution

Simultaneous solution of (2.9) and (2.10) was programmed as follows: The quantities ω and $f'(0)$ are given an initial guess. At $\zeta = \zeta_0 = 0$ the electron momenta p are known on the basis of their initial conditions, and they can be immediately averaged. The average value is used to perform one integration step ($\zeta_0 \rightarrow \zeta_1$) for the field profile starting with the boundary condition for it. After this, the resulting field at ζ_1 can be used for advancing the electrons one step from ζ_0 . At this point one complete integration step has been performed and it can be repeated over the whole resonator length.

At $\zeta = \zeta_{\text{out}}$ the boundary condition must be checked. To fulfill it, one changes the values given for ω and $f'(0)$ in analogy with the solution of the source-free field equation (2.12). Because the program spends most of its running time to solve the electron momenta, the number of different initial conditions was taken to be relatively small ($n_1 \approx 30$) during the iteration, and only finally it was increased ($n_2 = 360$) to achieve the desired resolution. It was found that even 10 electrons suffice to very accurately produce the same field profile that was obtained by taking several hundreds of electrons.

Fig. A.5 in Appendix A shows the flow chart the solution routine for one combination of control parameters I and Δ . A feasible initial guess for ω and $f'(0)$ is supposed to be given by the calling program.

4.5.2 Smoothness of the energy spectrum

To measure the complexity of the energy spectra of electrons exiting the resonator, we define a quantity

$$S = \int_0^{2\pi} \left| \frac{d|p(\zeta_{\text{out}})|}{d\vartheta_0} \right| d\vartheta_0, \quad (4.3)$$

which measures (twice) “the total amount of uphill and downhill” on the curve that shows the absolute value of final electron momenta as a function of the input phase. For a truly chaotic spectrum we would expect S to be infinite, a value which can not be found numerically. With a limited resolution on the ϑ_0 -axis we only can transform the qualitative nature of the spectrum into an approximate number. However, used with the perpendicular efficiency (which also is purely a function of the spectrum) the quantity S can be effectively exploited to classify the operating regions of a gyrotron.

4.5.3 Efficiency–smoothness plots

Cold-cavity approximation

The routines described above give the field profile and the electron momentum spectrum for a single combination of control parameters (F, Δ, μ) . We have a fixed cavity geometry described by the functions $R(\zeta)$ and $\chi(\zeta)$ shown in Fig. 4.3. For this particular cavity $\mu = 12.8$. The other two parameters were varied over the range of interest. The field $f(\zeta)$ is independent of Δ and F , so it needs not be recalculated every time. For each combination of Δ and F , the momentum spectrum is solved and the quantities η_{\perp} and S calculated from it. The results are then presented as contours of η_{\perp} and S in the (Δ, F) -plane, see Fig. 4.6. In Appendix A, Fig. A.3 shows the flow chart for this code.

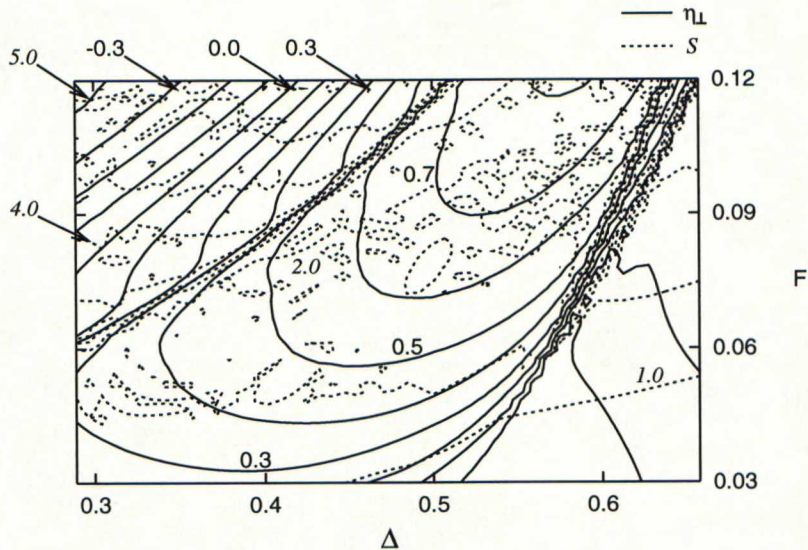


Figure 4.6: The contours of perpendicular efficiency η_{\perp} and smoothness S in the (Δ, F) -plane. The cold-cavity approximation has been used in the calculation.

Fig. 4.6 shows that the very smoothest energy spectra are obtained in the regions where the interaction is generally weak—which of course leads to low efficiency also. An example of this is the parameter combination $(\Delta = 0.6, F = 0.05)$. On the other hand, the efficiency is low in the vicinity of the upper left corner of the same plot. Here one can see traces of chaos: strong interaction and widely varying residual energies which explain the poor efficiency. Between these areas one finds the “normal” operating regime.

Inside it S increases (the spectrum becomes less smooth) with efficiency, but it has a reasonably low value throughout. Extreme sensitivity for initial conditions is seen in few cases only. To illustrate the electron energy spectra at different parts of the (Δ, F) -plane three representative points in it were chosen and the corresponding spectra plotted in Fig. 4.7.

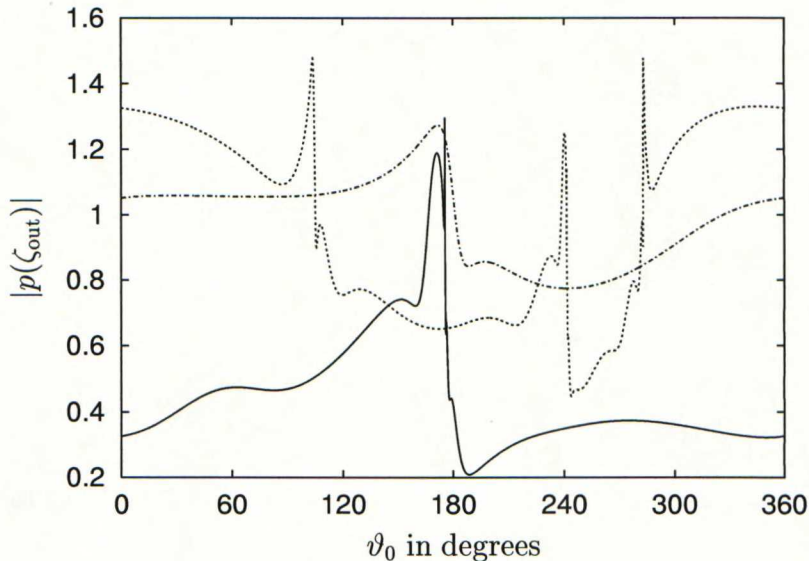


Figure 4.7: *Transverse momentum of electrons at the resonator end as a function of the initial angle. Solid: $\Delta = 0.55$, $F = 0.11$, $\eta_{\perp} = 0.78$, $S = 2.1$. Dash-dot: $\Delta = 0.60$, $F = 0.05$, $\eta_{\perp} \approx 0$, $S = 1.0$. Dotted: $\Delta = 0.35$, $F = 0.10$, $\eta_{\perp} \approx 0$, $S = 4.6$.*

Self-consistently calculated efficiency and smoothness

To self-consistently find the values of η_{\perp} and S corresponding to those presented in Fig. 4.6, more complicated computations than above are needed. For each point in the (Δ, I) -plane, one must solve both the field equation and the final momenta of electrons. As mentioned before, a feasible initial guess for the quantities ω and $f'(0)$ is needed in order to make the solver routine converge to the correct solution.

The fact that the eigenvalues ω and $f'(0)$ should depend on the control parameters Δ and I in a continuous manner was used. Once the solution in one point had been found, the values of ω and $f'(0)$ provided a good starting point for the next iteration with Δ and I sufficiently close to the previous values. Therefore the (Δ, I) -plane was scanned through along a

zigzag path, never jumping from one edge to the opposite one. A flow chart of this procedure is given in Fig. A.4 in Appendix A. Despite this approach, the program occasionally started following a false minimum of R [recall the definition (4.2) valid for the self-consistent calculation as well] and produced incorrect results. Therefore, the whole region of interest in the (Δ, I) -plane had to be divided into several rectangular areas. The routine was then run using a small number of electrons to manually find a promising initial guess for the first point in each box. Next, the boxes were scanned through one by one using a sufficient resolution in initial conditions (more electrons than at the first stage). Combining all data computed in this way, we obtain Fig. 4.8.

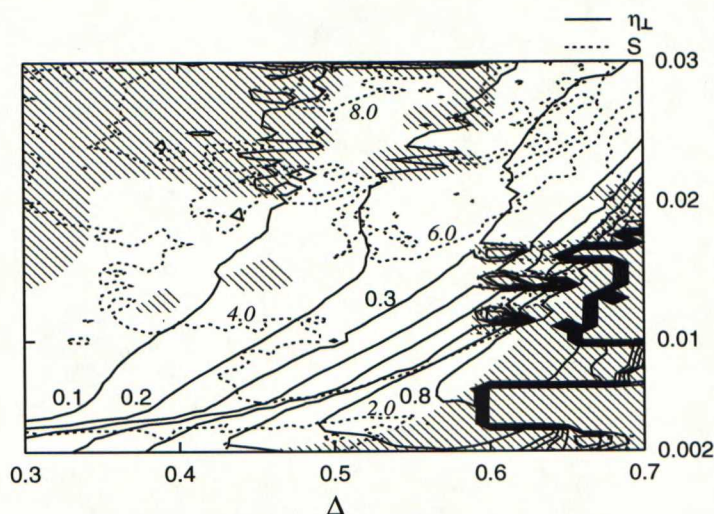


Figure 4.8: The contours of perpendicular efficiency η_{\perp} and smoothness S in (Δ, I) -plane. The calculation has been carried out self-consistently. Hatching indicates that a solution satisfying the boundary conditions for the field has not been found.

It seems that there are combinations of Δ and I for which no solution of the desired type exists. This suggestion is supported by the fact that in some cases a zero of R in $(\omega, f'(0))$ -plane ceases to have a zero in its neighborhood when Δ or I is slightly modified. Due to the complicated nature of the equations we are considering, this kind of bifurcations are impossible to study analytically. It has previously [47] been found, however, that a bifurcation of another type is shown by these equations. There are two distinct solutions—only one of which is physical—for sufficiently large values of I . The current study is restricted to these comments; the regions of the above-mentioned nature are indicated by hatching in Fig. 4.8.

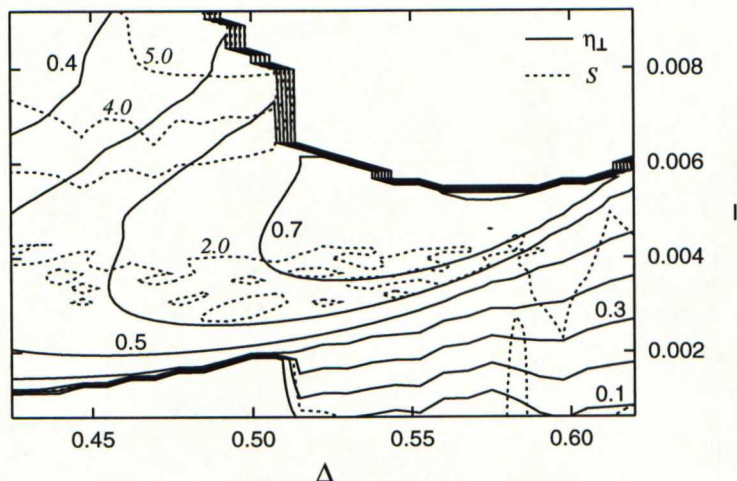


Figure 4.9: *The contours of the cold-cavity calculation presented in the (Δ, I) -plane for comparison with the self-consistent ones. Note the different scales on the axes.*

To compare the cold-cavity calculations with the self-consistent ones, the data shown in Fig. 4.6 was converted into another form using (2.15). The resulting plot is shown in Fig. 4.9. Note that only a small portion of the region included in Fig. 4.8 is covered.

Tapering of magnetic field

In [48] detailed studies of the influence of tapering of magnetic field on gyrotron efficiency and mode competition have been performed, but now the question arises what is the relation between this higher efficiency and the complexity of the corresponding electron energy spectrum. In principle the gyrotron equations (2.11)–(2.12) become a “less autonomous” system when dependence on ζ is allowed for Δ . We therefore expect it to be more inclined to behave chaotically.

We repeated the calculations which were carried out to produce Fig. 4.6 but used a non-uniform magnetic field:

- Linearly growing field with different slopes
- Parabolic field profile with a maximum in the middle of the resonator

No significant difference in the behavior of the gyrotron was found. As an example of these calculations, the contours of η_{\perp} and S calculated with a parabolic field are presented in Fig. 4.10.

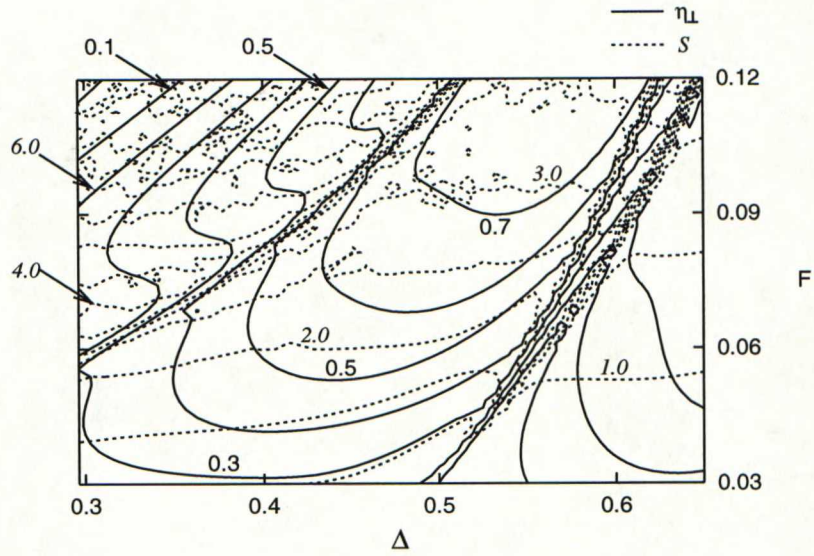


Figure 4.10: The contours of perpendicular efficiency η_{\perp} and smoothness S in the (Δ, F) -plane when the magnetic field has a parabolic profile with a 4 % tapering at both ends. The cold-cavity approximation has been used in the calculation. Compare to Fig. 4.6.

Chapter 5

Electron Trapping in a Gyrotron with a Depressed Collector

5.1 General

In a gyrotron with a depressed collector there is a risk for electrons to be reflected back towards the resonator by the retarding potential. This reflection takes place whenever the height of the potential barrier exceeds the longitudinal kinetic energy of an electron in the collector region. In [26] it was found via simulation that the electrons are eventually swept out to the collector by the high-frequency field, and no significant charge accumulation would thus result. However, how the reflected electrons affect the gyrotron efficiency has not been reported. The present work concentrates on this question.

5.2 Adiabatic and non-adiabatic trapping

Electron reflection by the retarding electrostatic potential can be regarded as an adiabatic process, if it takes place over a short distance compared to the Larmor period of the electron, that is, if $\Delta z_{\text{ret}} \ll z_L$ [27]. Here Δz_{ret} is the spatial extension of the retarding region, and $z_L = \mathcal{P}_{\parallel}/eB_{\text{coll}}$ is the Larmor period of an electron with a momentum component \mathcal{P}_{\parallel} in the direction of the magnetic field (B_{coll}) in the collector region. In this adiabatic case the reflected electron is expected to pass the resonator backwards, to reflect from the negative potential of the gun and to interact with the RF field again, following closely to the magnetic field lines on its way. This process continues until the electron's energy at the cavity end suffices to carry it to the collector.

Possible non-adiabaticity in the reflection tends to increase the transverse

momentum of the electron and, as a consequence, a reflection by the magnetic mirror of the increasing field before reaching the interaction cavity will result. As time goes on, diffusion across the magnetic field lines carries these electrons to the grounded body of the device [27]. This case will not be discussed further here.

5.3 Condition for electron trapping

To connect the retarding potential with the dimensionless momentum $p(\zeta_{\text{out}})$ obtained from the numerical computations, recall the normalization of the physical momenta given in Section 2.3: $|p| = \mathcal{P}_{\perp}/\mathcal{P}_{\perp 0}$ and $p_{\parallel} = \mathcal{P}_{\parallel}/\mathcal{P}_{\perp 0}$. For the sake of consistency, the notation p for the transverse momentum is used also in this context, even though the longitudinal momentum p_{\parallel} also appears in the calculations.

Using the relation between the total energy of an electron and the accelerating voltage U_{cath} ,

$$(\mathcal{P}_{\perp 0}^2 + \mathcal{P}_{\parallel 0}^2)c^2 + (m_e c^2)^2 = W_{\text{tot}}^2 = (m_e c^2 + eU_{\text{cath}})^2,$$

and equations for the momentum components as a function of the normalized velocities $\beta_{\perp 0}$ and $\beta_{\parallel 0}$,

$$\mathcal{P}_{\perp 0} = \beta_{\perp 0} \gamma_{\text{rel}} m_e c \quad \text{and} \quad \mathcal{P}_{\parallel 0} = \beta_{\parallel 0} \gamma_{\text{rel}} m_e c,$$

together with $\gamma_{\text{rel}} = (1 - \beta_{\parallel 0}^2 - \beta_{\perp 0}^2)^{-1/2}$ and the definition of the pitch factor $\alpha = \beta_{\perp 0}/\beta_{\parallel 0}$ we find that

$$\mathcal{P}_{\perp 0} = \alpha m_e c \sqrt{\frac{2\phi_{\text{cath}} + \phi_{\text{cath}}^2}{1 + \alpha^2}} \quad (5.1)$$

and

$$\mathcal{P}_{\parallel 0} = m_e c \sqrt{\frac{2\phi_{\text{cath}} + \phi_{\text{cath}}^2}{1 + \alpha^2}}. \quad (5.2)$$

Here $\phi_{\text{cath}} = eU_{\text{cath}}/m_e c^2$.

Between the cavity end and the retarding potential hill the electron experiences a diverging magnetic field but no electric field. Its total kinetic energy is therefore conserved,

$$\mathcal{P}_{\perp}(z)^2 + \mathcal{P}_{\parallel}(z)^2 = \text{const}, \quad (5.3)$$

but the transverse motion slows down along with the weakening of the magnetic field [27]:

$$\frac{\mathcal{P}_\perp(z)^2}{B(z)} = \text{const.} \quad (5.4)$$

In the vicinity of the collector the magnetic field B_{coll} is weak and practically constant. Applying these conservation laws at the cavity end ($z = z_{\text{out}}$, $B = B_{\text{cav}}$) and at the collector ($B = B_{\text{coll}}$), we obtain for the axial kinetic energy at the collector

$$W_\parallel(z_{\text{coll}}) = \sqrt{\left[\mathcal{P}_\parallel(z_{\text{out}})^2 + \left(1 - \frac{B_{\text{coll}}}{B_{\text{cav}}}\right) \mathcal{P}_\perp(z_{\text{out}})^2 \right] c^2 + (m_e c^2)^2 - m_e c^2},$$

which is available for surpassing the retarding potential U_{coll} . Those electrons for which

$$W_\parallel(z_{\text{coll}}) > eU_{\text{coll}},$$

reach the collector. For the absolute value of the (complex) dimensionless transverse momentum, $|p(\zeta_{\text{out}})| = \mathcal{P}_\perp(z_{\text{out}})/\mathcal{P}_{\perp 0}$, this condition reads

$$|p(\zeta_{\text{out}})| > \frac{m_e c}{\mathcal{P}_{\perp 0}} \sqrt{\frac{2\phi_{\text{coll}} + \phi_{\text{coll}}^2 - \mathcal{P}_{\parallel 0}^2/m_e^2 c^2}{1 - B_{\text{coll}}/B_{\text{cav}}}},$$

since $\mathcal{P}_\parallel(z_{\text{out}}) = \mathcal{P}_{\parallel 0}$. Substituting Eqs. (5.1) and (5.2), as well as $\phi_{\text{coll}} = eU_{\text{coll}}/m_e c^2$ and $\phi_{\text{cath}} = eU_{\text{cath}}/m_e c^2$, this critical value can be expressed as a function of the physical voltages, magnetic fields and the pitch factor:

$$\begin{aligned} |p(\zeta_{\text{out}})| &> \frac{1}{\alpha \sqrt{1 - B_{\text{coll}}/B_{\text{cav}}}} \sqrt{\frac{2eU_{\text{coll}}m_e c^2 + (eU_{\text{coll}})^2}{2eU_{\text{cath}}m_e c^2 + (eU_{\text{cath}})^2} (1 + \alpha^2) - 1} \\ &\equiv p_{\text{cut-off}}. \end{aligned} \quad (5.5)$$

We call the right-hand side $p_{\text{cut-off}}$ since all electrons with $|p(\zeta_{\text{out}})| < p_{\text{cut-off}}$ are “cut off” from the spectrum by reflection. In the case $2\phi_{\text{coll}} + \phi_{\text{coll}}^2 < \mathcal{P}_{\parallel 0}^2/m_e^2 c^2$ the initial longitudinal momentum alone suffices to bring the electron to the collector and we state that $p_{\text{cut-off}} = 0$. Since $B_{\text{coll}}/B_{\text{cav}} \ll 1$ in real gyrotrons, that term is neglected in the first square root, and $p_{\text{cut-off}}$ is calculated from the voltages and the pitch factor.

5.4 Effects of electron trapping on perpendicular efficiency

5.4.1 General efficiency plots with inclusion of trapping

Adiabatically reflected electrons follow the magnetic field lines through the resonator and reflect from the gun potential again. Interaction with the high-frequency field takes place during the passage through the cavity in both directions. It is possible that the electrons gain energy from the field so that they are capable of reaching the collector. If not, the process continues until the energy finally is sufficiently large.

It is worth noting that Eq. (2.11) is symmetric with respect to reversal of the direction of ζ . Indeed, if $p_1(\zeta)$ is the unique solution of (2.11) corresponding to the initial value $p_1(0) = p_0$, and $p_1(\zeta_{\text{out}}) = p_{\text{out}}$, then $\tilde{p}_1(\tilde{\zeta}) = p_1(\zeta)$ (where $\tilde{\zeta} = \zeta_{\text{out}} - \zeta$) will satisfy the initial value problem

$$\frac{dp}{d\tilde{\zeta}} = -ip(\Delta + |p|^2 - 1) + iF\tilde{f}(\tilde{\zeta}), \quad p(\tilde{\zeta} = 0) = p_{\text{out}}$$

and yield $\tilde{p}_1(\zeta_{\text{out}}) = p_0$ again. Here $\tilde{f}(\tilde{\zeta}) = f(\zeta)$. We used this property to test the integration routine and were able to reproduce most initial conditions to high accuracy. Only very close to the points of suspected chaotic nature there was significant deviation, which fits well in the picture. If the true solution is sensitively dependent on initial conditions, no numerical routine can be expected to solve it to arbitrary accuracy.

We model the process of successive interactions and reflections by integrating numerically the gyrotron equation in the cold-cavity approximation, starting as in Section 4.5 and repeating the integration as many times as needed. To make the results general, a Gaussian field profile (2.13) is used. The motion of an electron traveling backwards in the resonator can be most conveniently found by performing the integration with the standard routine from $\zeta = \zeta_{\text{out}}$ to $\zeta = \zeta_0 = 0$ with a negative step size (see Fig. A.1 in Appendix A).

The time that the electrons spend outside the resonator between two successive interactions is long compared to their Larmor period. We therefore completely lose the information about the phase of rotation. The energy, instead, is conserved due to the assumption of adiabaticity. These facts are taken into account by keeping the absolute value of the momentum fixed and randomizing the phase angle each time before starting a new integration.

The results are presented as contour plots of perpendicular efficiency η_{\perp} in the (μ, F) -plane, see Figs. 5.1–5.3. The first of these figures is just the

standard plot with $p_{\text{cut-off}} = 0$. The parameter Δ is set in each point to the optimum value with respect to perpendicular efficiency when no trapping is taken into consideration. These values of Δ are then used for all different $p_{\text{cut-off}}$. A complete flow chart for the whole procedure is shown in Fig. A.6 in Appendix A.

When studying Figs. 5.1–5.3, the region close to the upper right corner of the grid should be neglected. The gyrotron parameter space defined by F and μ has more than one high-efficiency region. Around the efficiency maximum at the center of Fig. 5.1 the technological constraints are most easily satisfied, and it is unclear whether a device operating at the other (even higher) maxima could be designed. For example, at $(\mu \approx 25, F \approx 0.30)$ there is a second high-efficiency region which is more susceptible to velocity spread and space charge effects. [49]

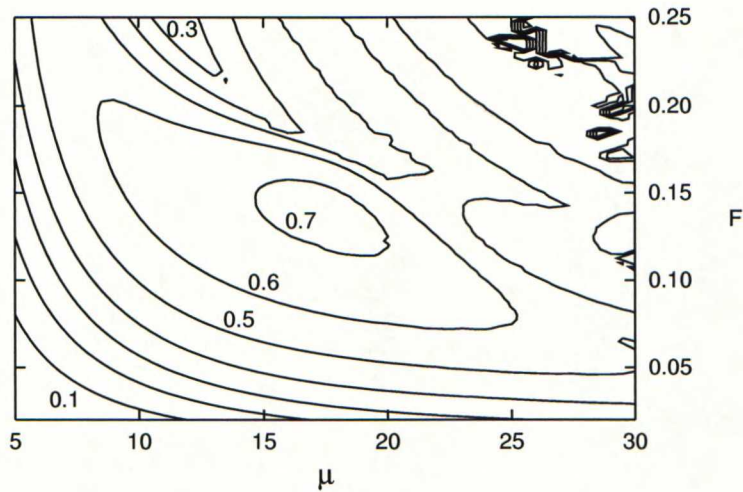


Figure 5.1: The contours of perpendicular efficiency η_{\perp} with $p_{\text{cut-off}} = 0$.

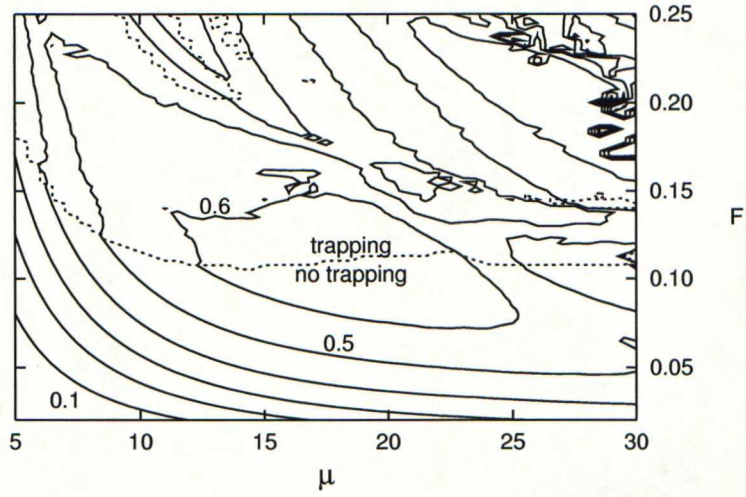


Figure 5.2: The contours of perpendicular efficiency η_{\perp} with $p_{\text{cut-off}} = 0.2$. The dashed line is the boundary between the regions with and without trapping.

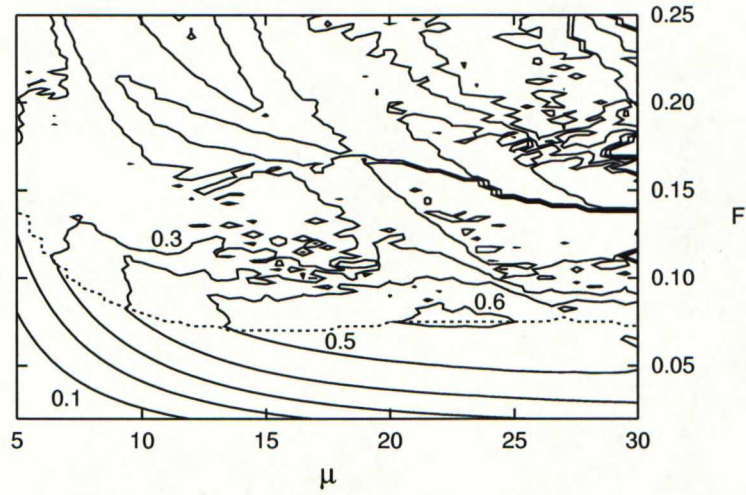


Figure 5.3: The contours of perpendicular efficiency η_{\perp} with $p_{\text{cut-off}} = 0.4$. The dashed line is the boundary between the regions with (above) and without trapping (below).

5.4.2 Dependence of efficiency on collector potential

General

It is evident from Figs. 5.1–5.3 that the favorable effect of a depressed collector on total efficiency will be limited by too high values of $p_{\text{cut-off}}$, that is, too high retarding voltages. Due to the general nature of the plots 5.1–5.3, they are not the most handy way of finding out the maximum reasonable retarding voltage for a specific gyrotron. The formalism developed in this chapter, however, allows this to be done, and it will be illustrated by choosing three representative points in the (μ, F) -plane and calculating explicitly the overall efficiency as a function of the retarding voltage. To do this, the values of U_{cath} and α were fixed to 90 kV and 1.5, respectively, which are typical for modern high-power gyrotrons.

In the following, a spread in the transverse velocity of the electrons is introduced. The results of this section are presented with inclusion of the spread. However, in each of Figs. 5.4–5.9 the dependence obtained for an ideal beam is also included. A reader who is only interested in seeing the effect of trapping in its most reduced form may skip this discussion and concentrate on studying the curves with $\delta\beta_{\perp} = 0\%$.

Inclusion of electron velocity spread

In practice it is impossible to produce an electron beam in which all electrons would have the same transverse and axial velocities when they are emitted from the cathode. In this context this is also taken into account. We handle the transverse velocity spread of electrons in line with [17]—utilizing the fact that the control parameters of the gyrotron change with the transverse velocity. This means that in reality the gyrotron always operates with several combinations of μ , F , and Δ simultaneously, and its efficiency is the average of all resulting efficiencies.

The quantities μ , F , and Δ can be expressed as

$$\mu = C_{\mu}^{\beta} \frac{\beta_{\perp}^2}{\beta_{\parallel}}, \quad (5.6)$$

$$F = \frac{C_F^{\beta}}{\beta_{\perp}^3}, \quad (5.7)$$

$$\Delta = \frac{C_{\Delta}^{\beta}}{\beta_{\perp}^2}, \quad (5.8)$$

where C_μ^β , C_F^β , and C_Δ^β do not depend on β_\perp . The longitudinal velocity β_\parallel can be written using the perpendicular velocity β_\perp and the relativistic factor γ_{rel} of the electrons as $\beta_\parallel = (1 - 1/\gamma_{\text{rel}}^2 - \beta_\perp^2)^{1/2}$. Introducing the error ϵ of the transverse velocity we find that the operating parameters μ_ϵ^β , F_ϵ^β , Δ_ϵ^β , and the pitch factor α_ϵ^β corresponding to ϵ are

$$\mu_\epsilon^\beta = C_\mu^\beta \frac{\beta_{\perp 0}^2 (1 + \epsilon)^2}{\sqrt{1 - 1/\gamma_{\text{rel}}^2 - \beta_{\perp 0}^2 (1 + \epsilon)^2}}, \quad (5.9)$$

$$F_\epsilon^\beta = \frac{C_F^\beta}{\beta_{\perp 0}^3 (1 + \epsilon)^3}, \quad (5.10)$$

$$\Delta_\epsilon^\beta = \frac{C_\Delta^\beta}{\beta_{\perp 0}^2 (1 + \epsilon)^2}, \quad (5.11)$$

$$\alpha_\epsilon^\beta = \frac{\beta_{\perp 0} (1 + \epsilon)}{\sqrt{1 - 1/\gamma_{\text{rel}}^2 - \beta_{\perp 0}^2 (1 + \epsilon)^2}}. \quad (5.12)$$

These can be written as

$$\mu_\epsilon^\beta = \frac{\mu (1 + \epsilon)^2}{\sqrt{1 - 2\alpha^2 \epsilon - \alpha^2 \epsilon^2}}, \quad (5.13)$$

$$F_\epsilon^\beta = \frac{F}{(1 + \epsilon)^3}, \quad (5.14)$$

$$\Delta_\epsilon^\beta = \frac{\Delta}{(1 + \epsilon)^2}, \quad (5.15)$$

$$\alpha_\epsilon^\beta = \frac{\alpha (1 + \epsilon)}{\sqrt{1 - 2\alpha^2 \epsilon - \alpha^2 \epsilon^2}}. \quad (5.16)$$

We computed the electron efficiency as a function of the retarding voltage for the chosen combinations of μ and F [$(\mu = 10, F = 0.10)$, $(\mu = 17, F = 0.125)$, $(\mu = 25, F = 0.075)$], simultaneously introducing a spread

in the electron transverse velocity. This was done by applying (5.5) with (5.13)–(5.16). A Gaussian

$$f_e(\beta_\perp) = \frac{1}{\sigma\sqrt{2\pi}} \exp\left[-\frac{(\beta_\perp - \beta_{\perp 0})^2}{2\sigma^2}\right] \quad (5.17)$$

is a suitable approximation for the velocity distribution [50]. The relation between the RMS deviation σ and the velocity spread $\delta\beta_\perp$ can be written as

$$\delta\beta_\perp = 1.8\sqrt{2}\sigma, \quad (5.18)$$

where $\delta\beta_\perp$ is defined as

$$\delta\beta_\perp = \frac{1}{2} \left(\frac{\beta_{\perp, \max} - \beta_{\perp, \min}}{\beta_{\perp, \text{center}}} \right). \quad (5.19)$$

In addition to an ideal beam with zero spread we used $\delta\beta_\perp = 10\%$ and 20% . The corresponding values of σ are 0.0393 and 0.0786. From (5.13) it follows that $|\epsilon|$ must be smaller than $\epsilon_{\max} = (1 + 1/\alpha^2)^{1/2}$, which is related to the fact that the physical boundaries of β_\perp are $0 \leq \beta_\perp \leq (1 - 1/\gamma_{\text{rel}}^2)^{1/2}$. In practice the efficiency was calculated by varying ϵ between $-0.95\epsilon_{\max}$ and $+0.95\epsilon_{\max}$ and averaging the corresponding efficiencies with a properly normalized weight function of the form (5.17). This method is an equivalent alternative for the Monte Carlo approach used in [17]. However, it suffers less from random fluctuations with equal computational effort.

As in [17], the quantities μ_ϵ^β , F_ϵ^β , and Δ_ϵ^β were treated as statistically independent variables assigning a different ϵ to each of them. This independence of errors for the three quantities μ , F , and Δ simulates the fact that in real gyrotrons a change of β_\perp always influences other operating parameters. For example, the field profile (the effective length of the cavity), the quality factor of the cavity, and the operation frequency depend on the properties of the electron beam, which means that the parameters μ , F , and Δ in fact are complicated functions of β_\perp . Quantitatively this could be taken into account only in self-consistent calculations, which is beyond the scope of this theory. The results of the present calculations are shown in Figs. 5.4–5.6.

However, if we make the most conservative but a less realistic assumption that the variation of β_\perp does not affect any other quantity, we should use one and the same ϵ in calculating μ_ϵ^β , F_ϵ^β , Δ_ϵ^β , and α_ϵ^β according to Eqs. (5.13)–(5.16). In this approach, which we call statistically dependent, we also calculated $p_{\text{cut-off}}$ from (5.5) for each β_\perp using the corrected α of Eq. (5.16). The results of such calculations are presented in Figs. 5.7–5.9.

It is obvious that here the efficiency deterioration due to velocity spread is much smaller than in the former case.

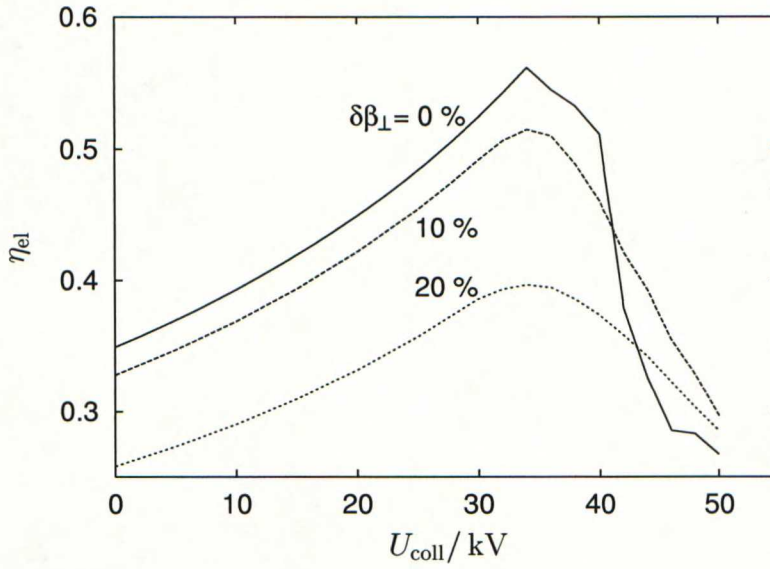


Figure 5.4: *The total electron efficiency as a function of retarding potential at $\mu = 10.0$ and $F = 0.10$, calculated with statistically independent variables.*

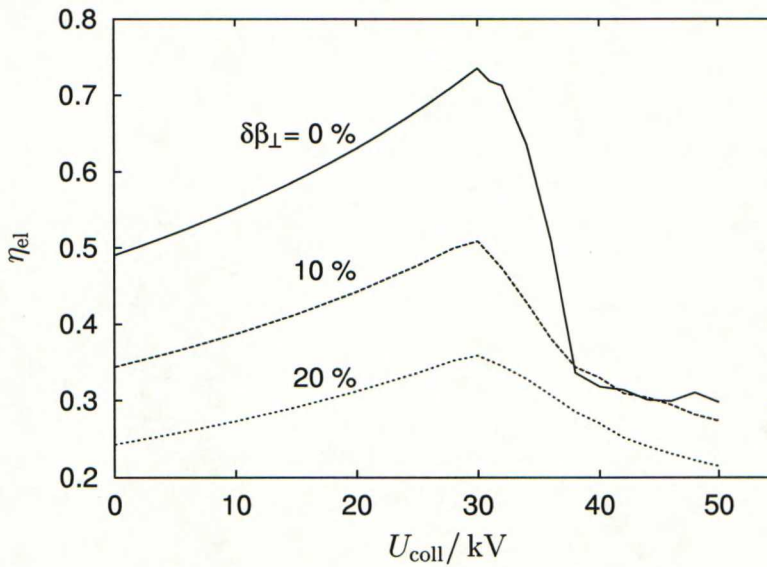


Figure 5.5: *The total electron efficiency as a function of retarding potential at $\mu = 17.0$ and $F = 0.125$, calculated with statistically independent variables.*

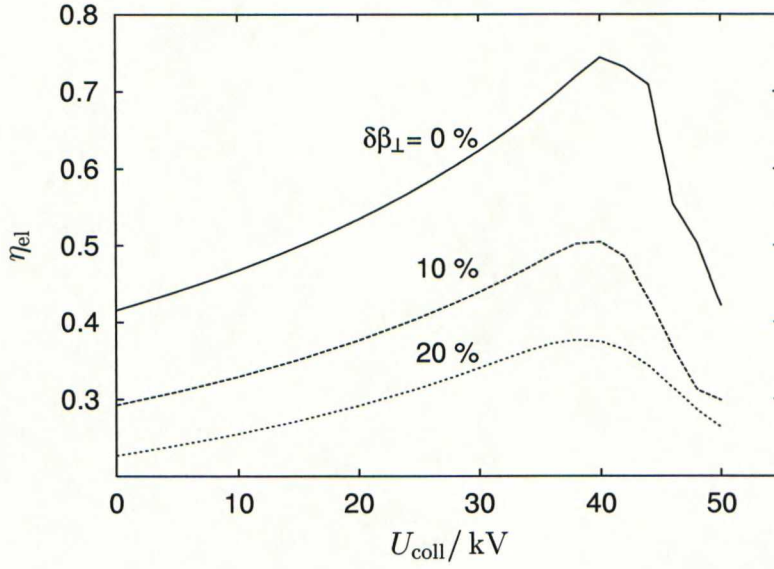


Figure 5.6: *The total electron efficiency as a function of retarding potential at $\mu = 25.0$ and $F = 0.075$, calculated with statistically independent variables.*

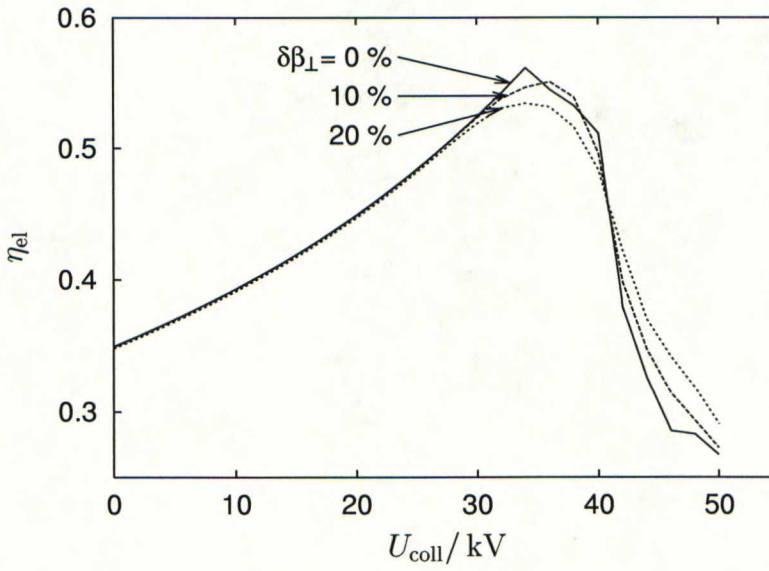


Figure 5.7: *Same as Fig. 5.7, but with statistically dependent variables.*

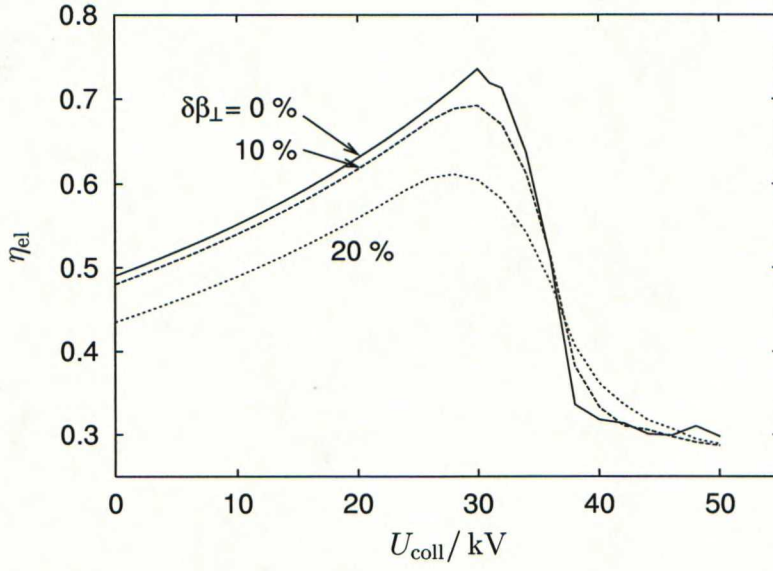


Figure 5.8: Same as Fig. 5.8, but with statistically dependent variables.

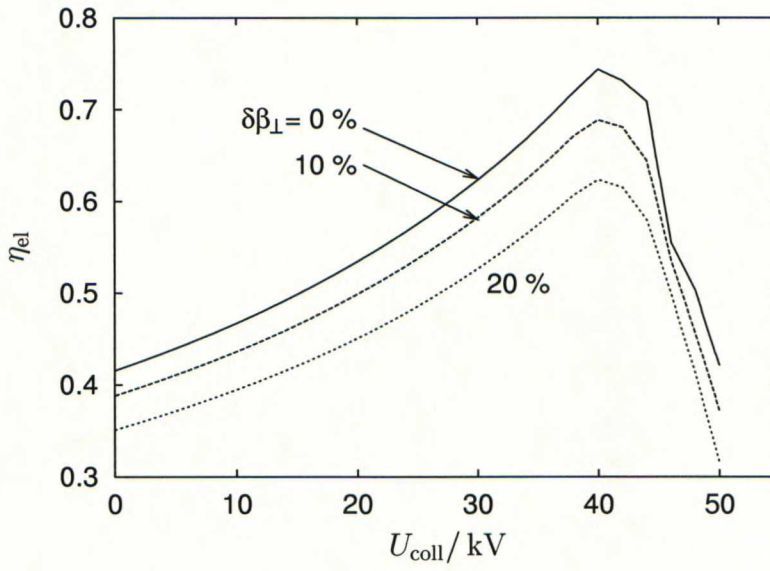


Figure 5.9: Same as Fig. 5.9, but with statistically dependent variables.

5.4.3 Space charge effects

One should be concerned about additional space charge in the resonator if there is a large fraction of electrons bouncing through it several times. In the computations of Section 5.4.1 the average number of interactions at each point in (μ, F) -plane was also recorded, and the results for $p_{\text{cut-off}} = 0.2$ are shown in Fig. 5.10. If we take $U_{\text{coll}} = 90 \text{ kV}$ and $\alpha = 1.5$ as in Sec. 5.4.2, this value of $p_{\text{cut-off}}$ corresponds to $U_{\text{cath}} = 39 \text{ kV}$.

It is seen from Fig. 5.10 that the amount of electrons in the resonator does not increase very much due to the trapping effect, even though a relatively high retarding voltage has been applied.

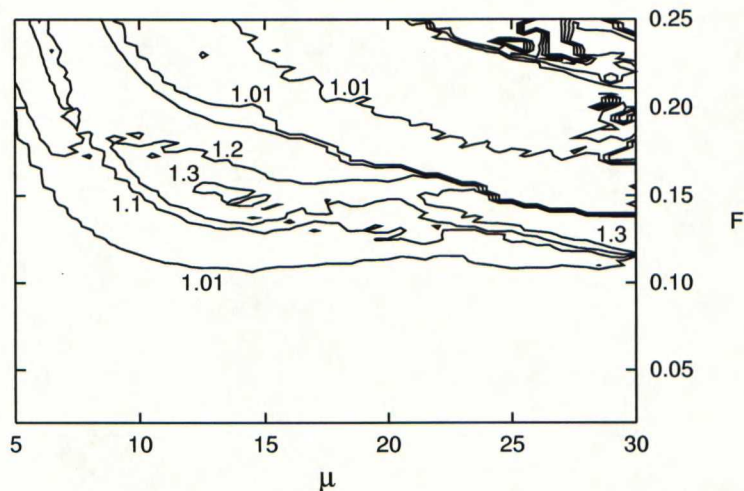


Figure 5.10: The number of interactions averaged over all electrons at different values of μ and F with $p_{\text{cut-off}} = 0.2$.

Chapter 6

Conclusions

6.1 Chaotic electron trajectories

Electron residual energy spectra were computed numerically using the cold-cavity approximation in Chapter 4. The validity of this approximation was checked by solving a sample problem in parallel with a self-consistent model. The good agreement between the two models showed the cold-cavity approximation to be a feasible one, and, therefore, a natural choice due to its practical benefits. The self-consistent computations are more complicated to perform and computationally considerably more expensive than the ones needed within the cold-cavity approximation.

Using the results, we can classify the operating regimes of a gyrotron as follows. The operation parameter plane (Δ , F) is divided into three different parts using the concepts of perpendicular efficiency η_{\perp} and smoothness S :

- The region of a high η_{\perp} and a relatively low S . The value of S increases (the spectrum becomes less smooth) with efficiency, but it has a reasonably low value throughout. Strong sensitivity for initial conditions is seen in few cases only.
- The region of weak interaction that makes both η_{\perp} and S remain low. The dependence of electron residual energies on their initial conditions is also weak everywhere.
- The region of strong interaction with a low η_{\perp} and a high S . Extreme dependence on initial conditions is common. Residual energies have a strong variation, which explains the poor efficiency.

The three regions are separated by rather sharp boundaries. It makes sense to operate the gyrotron only in the first region, which is located between

the two other ones in the (Δ, F) -plane. The region of weak interaction can not provide an efficiency good enough, even though it might seem attractive from the viewpoint of the use of depressed collectors. The high-interaction regime, on the other hand, is inferior to the “normal” one with respect to both η_{\perp} and S . All these findings remain valid when the guiding magnetic field is allowed to vary over the interaction cavity.

6.2 Electron trapping

In Chapter 5 the electrostatic trapping of electrons in the presence of a depressed collector was studied. A formalism was developed for inclusion of the trapping into gyrotron efficiency calculations. Several representative sets of gyrotron parameters were chosen as examples.

It is evident from Figs. 5.2 and 5.3 that the trapping effect is more probable and pronounced in the operating regimes with a high perpendicular efficiency. Indeed, here many electrons have very low residual energies at the exit from the cavity. They make largest contributions to efficiency. At the same time these “good” electrons have the strongest tendency to become trapped. For example, at the point of the highest efficiency ($\mu = 17$, $F = 0.125$) with $U_{\text{coll}} = 33$ kV some of the “best” electrons pass the cavity six times before they acquire the energy from the RF field which is needed for leaving the trap. It is also seen (Figs. 5.5 and 5.8) that just for these μ and F values the increase of the efficiency due to the retarding potential as $U_{\text{cath}}/(U_{\text{cath}} - U_{\text{coll}})$ breaks down already at ~ 30 kV because of the onset of trapping, while in two other cases trapping begins to manifest itself at higher collector voltages. It is also observed that generally the velocity spread tends to smooth the transition to the trapping region.

In gyrotrons whose cavities have a low quality factor the dependences shown in Figs. 5.4–5.6 should be observed, while in the case of high quality factors weaker dependence on the velocity spread such as shown in Figs. 5.7–5.9 should be expected.

The space charge effects resulting from trapped electrons in the resonator were found to be of minor importance. Whenever the cold-cavity approximation is valid for the regular solution of the gyrotron equations, it will also be applicable in the trapping computations, since the magnitude of space charge in the resonator remains essentially the same. On the other hand, reflected electrons traveling backwards in the beam tunnel might slightly increase the velocity spread of electrons. This effect could be described within the kinetic approach, which is beyond the scope of the present investigations.

6.3 Recommendations

When applying a single-stage depressed collector to a gyrotron, the collector potential should be chosen such that even the least energetic electrons of the spent beam can reach the collector. Typically, the maximum applicable voltage is between 30 and 40 kV. To find out the exact value of the maximum voltage for a specific gyrotron, the methods introduced in this thesis can be used. The next step in future work is to create a collection of “efficiency vs. retarding voltage” graphs for existing gyrotrons.

Required that extensive electron trapping has been avoided by a suitable choice of the retarding potential, the gyrotron achieves its maximum efficiency using the same operating parameters as without the collector potential depression.

Parts of the present work will be published in [41] and [51].

Bibliography

- [1] M. Airila *et al.*, in *Proceedings of the XXXIV Annual Conference of the Finnish Physical Society, Helsinki University of Technology Publications in Engineering Physics*, Helsinki University of Technology, edited by M. Kaivola and E. Noponen (Otamedia Oy, Espoo, 2000), p. 158.
- [2] J. G. Cordey, R. J. Goldston, and R. R. Parker, *Phys. Today* **45**, 22 (1992).
- [3] A. Phelps, in *Generation and Application of High Power Microwaves*, The Institute of Physics, edited by R. A. Cairns and A. D. R. Phelps (Institute of Physics Publishing, Bristol, 1997).
- [4] N. J. Fisch, in *Generation and Application of High Power Microwaves*, The Institute of Physics, edited by R. A. Cairns and A. D. R. Phelps (Institute of Physics Publishing, Bristol, 1997).
- [5] K. I. Thomassen, *J. Fusion Energy* **9**, (1990).
- [6] M. Thumm, *Fusion Eng. Des.* **30**, 139 (1995).
- [7] J. Koponen, Master's thesis, Helsinki University of Technology, Espoo, 1995.
- [8] M. Thumm, Technical Report No. FZKA 5564, Forschungszentrum Karlsruhe—Technik und Umwelt, Karlsruhe (unpublished).
- [9] W. M. Manheimer, *Int. J. Electron.* **72**, 1165 (1992).
- [10] O. Dumbrajs and M. Thumm, *Int. J. Electron.* **76**, 351 (1994).
- [11] V. L. Granatstein, R. K. Parker, and C. M. Armstrong, *Proc. IEEE* **87**, 702 (1999).
- [12] C. J. Edgcombe, in *Gyrotron Oscillators—Their Principles and Practice*, edited by C. J. Edgcombe (Taylor & Francis, London, 1993), pp. 1–8.

- [13] R. Advani *et al.*, in *Twenty Fourth International Conference on Infrared and Millimeter Waves—Conference Digest*, University of California, edited by L. A. Lombardo (University of California, Davis, 1999).
- [14] C. T. Iatrou *et al.*, Technical report, European Commission (unpublished).
- [15] A. van der Ziel, *Solid State Physical Electronics* (Prentice-Hall, Englewood Cliffs, 1957).
- [16] B. Piosczyk, in *Gyrotron Oscillators—Their Principles and Practice*, edited by C. J. Edgcombe (Taylor & Francis, London, 1993), pp. 123–146.
- [17] O. Dumbrajs and J. P. T. Koponen, *Phys. Plasmas* **6**, 2618 (1999).
- [18] R. S. Symons and H. R. Jory, in *Advances in Electronics and Electron Physics*, edited by L. Marton and C. Marton (Academic Press, New York, 1981), Vol. 55, pp. 1–75.
- [19] P. Sprangle and A. T. Drobot, *IEEE Trans. Microwave Theory Tech.* **25**, 528 (1977).
- [20] M. Thumm, Technical Report No. FZKA 5877, Forschungszentrum Karlsruhe—Technik und Umwelt, Karlsruhe (unpublished).
- [21] J. Feinstein and K. Felch, *IEEE Trans. Electron Dev.* **ED-34**, 461 (1987).
- [22] V. A. Flyagin, A. V. Gaponov, M. I. Petelin, and V. K. Yulpatov, *IEEE Trans. Microwave Theory Tech.* **25**, 514 (1977).
- [23] V. L. Bratman, M. A. Moiseev, and M. I. Petelin, in *Gyrotrons: Collected Papers*, edited by A. Gaponov-Grekhov (Institute of Applied Physics, Russian Academy of Sciences, Nizhny Novgorod, 1981), pp. 104–121.
- [24] G. S. Nusinovich and R. E. Erm, *Elektronnaya Tekhnika, Seriya I, Elektronika SVCh* **8**, 55 (1972).
- [25] N. A. Zavolsky, G. S. Nusinovich, and A. B. Pavelyev, *Radiofizika* **31**, 361 (1988).
- [26] K. Sakamoto *et al.*, *Phys. Rev. Lett.* **73**, 3532 (1994).
- [27] B. Piosczyk, C. T. Iatrou, G. Dammertz, and M. Thumm, *IEEE Trans. Plasma Sci.* **24**, 579 (1996).

- [28] N. P. Venediktov, M. Y. Glyavin, V. E. Zapevalov, and A. N. Kuftin, *Radiophys. Quant. Electron.* **41**, 449 (1998).
- [29] A. Singh, D. S. Weile, S. Rajapatirana, and V. L. Granatstein, *IEEE Trans. Plasma Sci.* **25**, 480 (1997).
- [30] G. Dammertz, in *Gyrotron Oscillators—Their Principles and Practice*, edited by C. J. Edgcombe (Taylor & Francis, London, 1993), pp. 147–178.
- [31] M. E. Read and A. J. Dudas, in *Thirteenth International Conference on Infrared and Millimeter Waves*, edited by R. J. Temkin (SPIE—The International Society for Optical Engineering, Honolulu, 1988), pp. 181–182.
- [32] M. E. Read, W. G. Lawson, A. J. Dudas, and A. Singh, *IEEE Trans. Electron Devices* **37**, 1579 (1990).
- [33] A. Singh *et al.*, *IEEE Trans. Plasma Sci.* **27**, 490 (1999).
- [34] A. S. Fix *et al.*, *Int. J. Electronics* **57**, 821 (1984).
- [35] T. V. Borodacheva, A. L. Goldenberg, and V. N. Manuilov, in *Gyrotrons*, edited by V. A. Flyagin (Institute of Applied Physics, Russian Academy of Sciences, Nizhny Novgorod, 1989), pp. 161–180, in Russian.
- [36] A. Singh, W. W. Destler, V. L. Granatstein, and W. R. Hix, *Int. J. Electron.* **72**, 827 (1992).
- [37] P. Ramins and B. T. Ebiara, *IEEE Trans. Electron Devices* **36**, 817 (1989).
- [38] K. L. Felch *et al.*, *Proc. IEEE* **87**, 752 (1999).
- [39] P. A. Lindsay and X. Chen, *IEEE Trans. Plasma Sci.* **22**, 834 (1994).
- [40] O. Dumbrajs, R. Meyer-Spasche, and A. Reinfelds, *IEEE Trans. Plasma Sci.* **26**, 846 (1998).
- [41] M. I. Airila, O. Dumbrajs, A. Reinfelds, and D. Teychenné, *Int. J. Infrared Millimeter Waves* **21**, No. 11 (2000), in press.
- [42] H. J. Korsch and H.-J. Jodl, *Chaos—A Program Collection for the PC*, 2nd ed. (Springer-Verlag, Berlin, 1999).

- [43] W. E. Boyce and R. C. DiPrima, *Elementary Differential Equations and Boundary Value Problems*, 5th ed. (John Wiley & Sons, New York, 1992).
- [44] R. L. Devaney, *An Introduction to Chaotic Dynamical Systems*, 2nd ed. (Addison-Wesley, New York, 1989).
- [45] A. M. Stuart and A. R. Humphries, *Dynamical Systems and Numerical Analysis* (Cambridge University Press, New York, 1996).
- [46] E. Borie, in *Gyrotron Oscillators—Their Principles and Practice*, edited by C. J. Edgcombe (Taylor & Francis, London, 1993), pp. 45–86.
- [47] H. Wenzelburger, Technical report, Kernforschungszentrum Karlsruhe (unpublished).
- [48] O. Dumbrajs, *Int. J. Electron.* **70**, 1131 (1991).
- [49] B. G. Danly and R. J. Temkin, *Phys. Fluids* **29**, 561 (1986).
- [50] V. E. Zapevalov, V. N. Manuilov, and S. E. Tsimring, *Izv. Vyssh. Uchebn. Zaved. Radiofiz.* **33**, 1406 (1990), [*Sov. Radiophys. and Quantum Electron.*].
- [51] M. I. Airila and O. Dumbrajs, *Phys. Plasmas*, submitted for publication (2000).

Appendix A

Flow Charts of the Numerical Codes

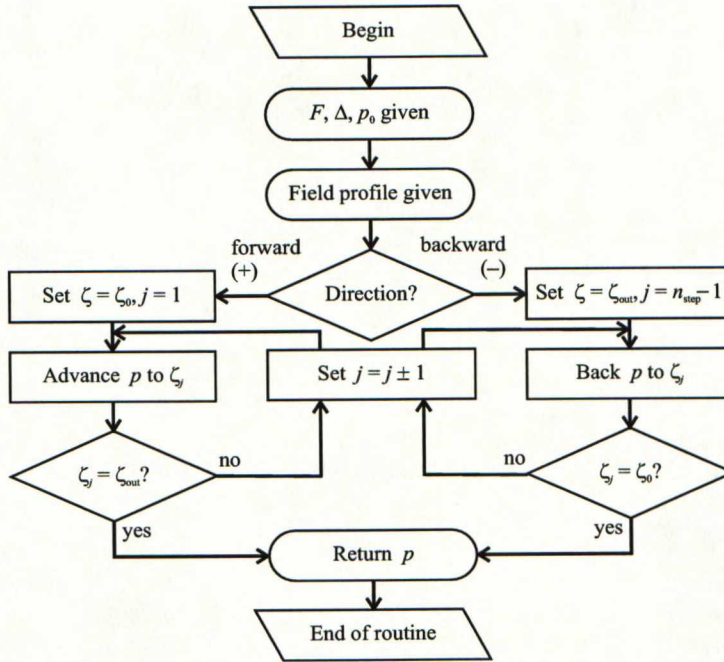


Figure A.1: Flow chart for the routine solving the gyrotron equation (2.11) in the cold-cavity approximation for a single initial condition $p(0) = p_0$ and a single combination of control parameters Δ and F . The high-frequency field profile is obtained from a separate routine, whose flow chart is presented in Fig. A.2.

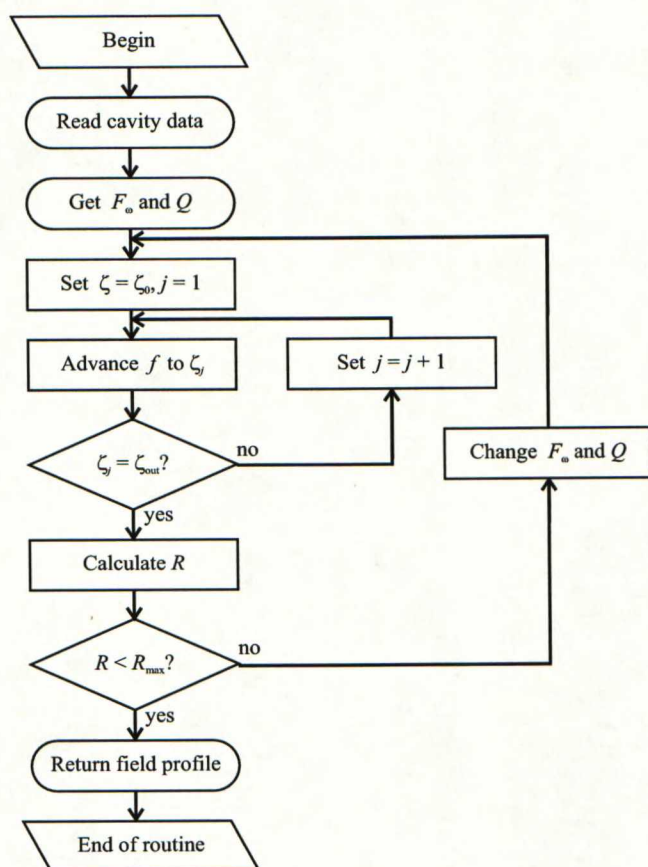


Figure A.2: Flow chart for the routine solving the high-frequency field profile $f(\zeta)$ in the cold-cavity approximation from Eq. (2.12).

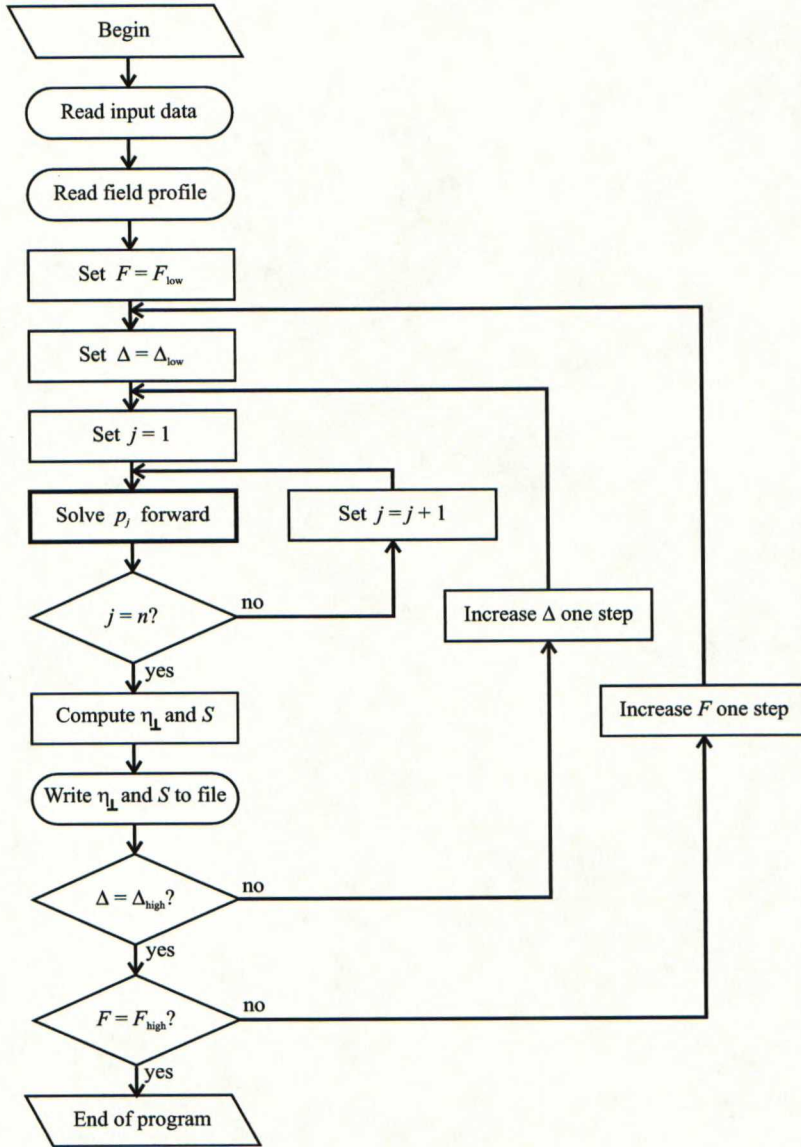


Figure A.3: Flow chart for the program performing the solution of the gyrotron equation in the cold-cavity approximation and calculating η_{\perp} and S for $\Delta_{\text{low}} \leq \Delta \leq \Delta_{\text{high}}$, $F_{\text{low}} \leq F \leq F_{\text{high}}$. The routine for the solution itself is written out separately in Fig. A.1.

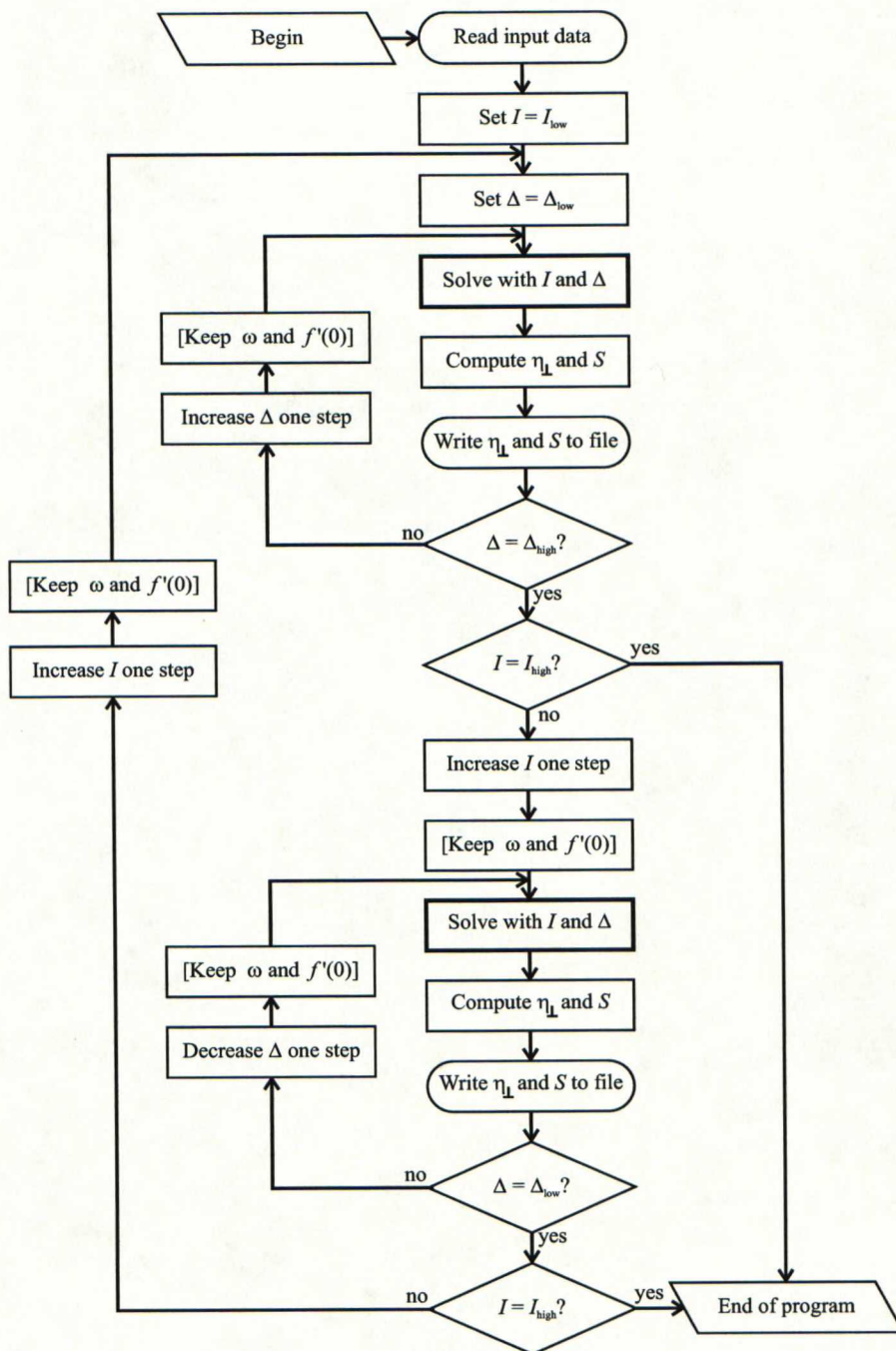


Figure A.4: Flow chart for the program solving the self-consistent gyrotron equations and calculating η_{\perp} and S for $\Delta_{\text{low}} \leq \Delta \leq \Delta_{\text{high}}$, $I_{\text{low}} \leq I \leq I_{\text{high}}$. The routine for the solution itself is written out separately in Fig. A.5.

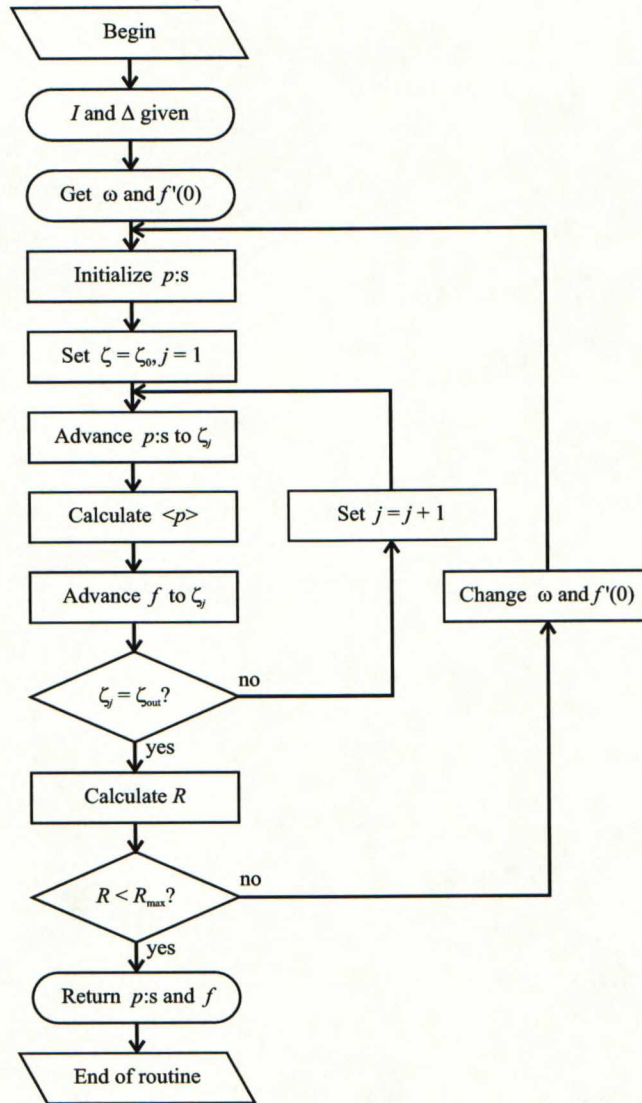


Figure A.5: Flow chart for the routine solving the self-consistent gyrotron equations for a single combination of control parameters Δ and I .

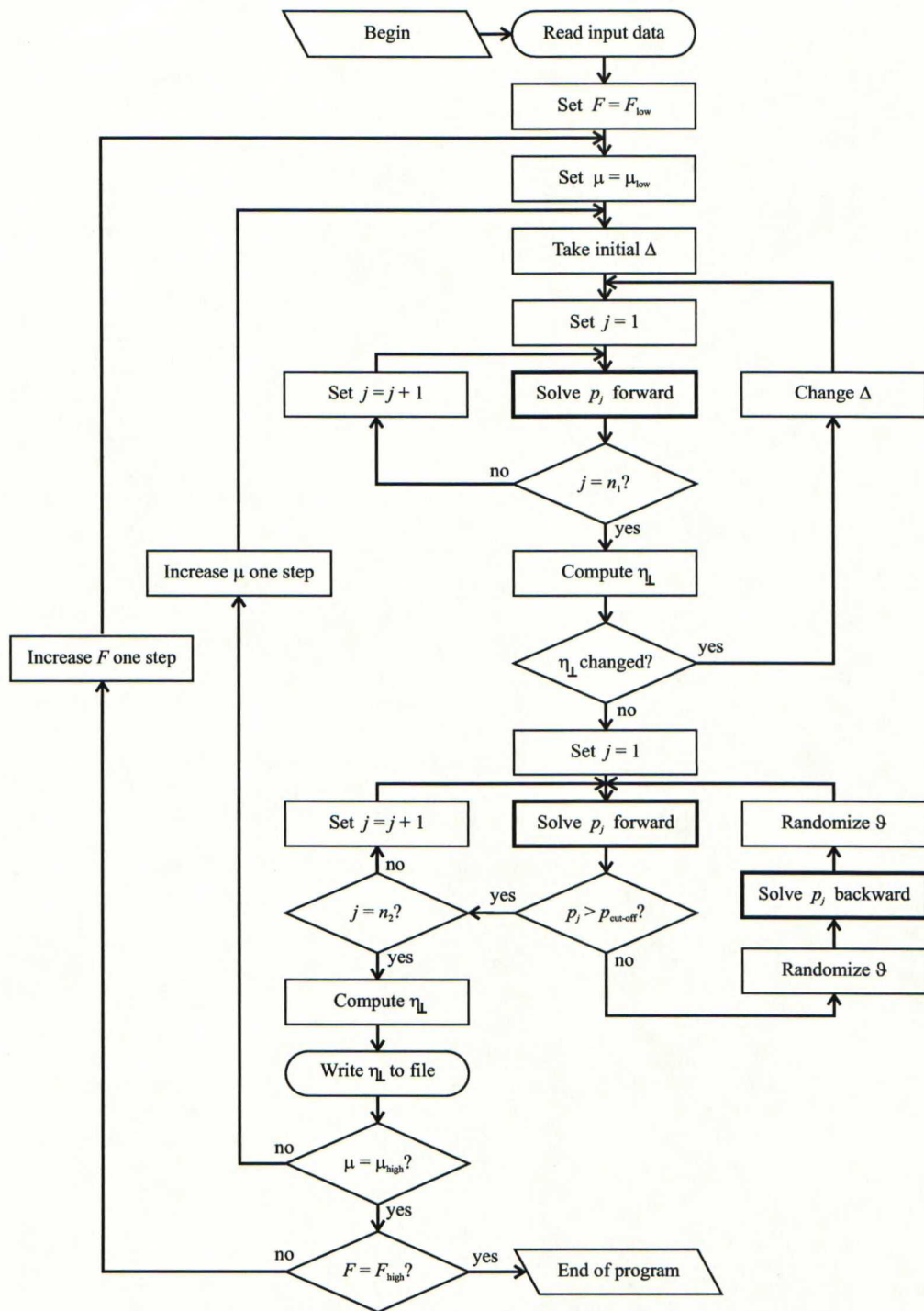


Figure A.6: Flow chart for the program solving the gyrotron equations and calculating η_{\perp} for $F_{low} \leq F \leq F_{high}$, $\mu_{low} \leq \mu \leq \mu_{high}$ when electron trapping due to a depressed collector is allowed. The routine for the solution itself is written out separately in Fig. A.1.